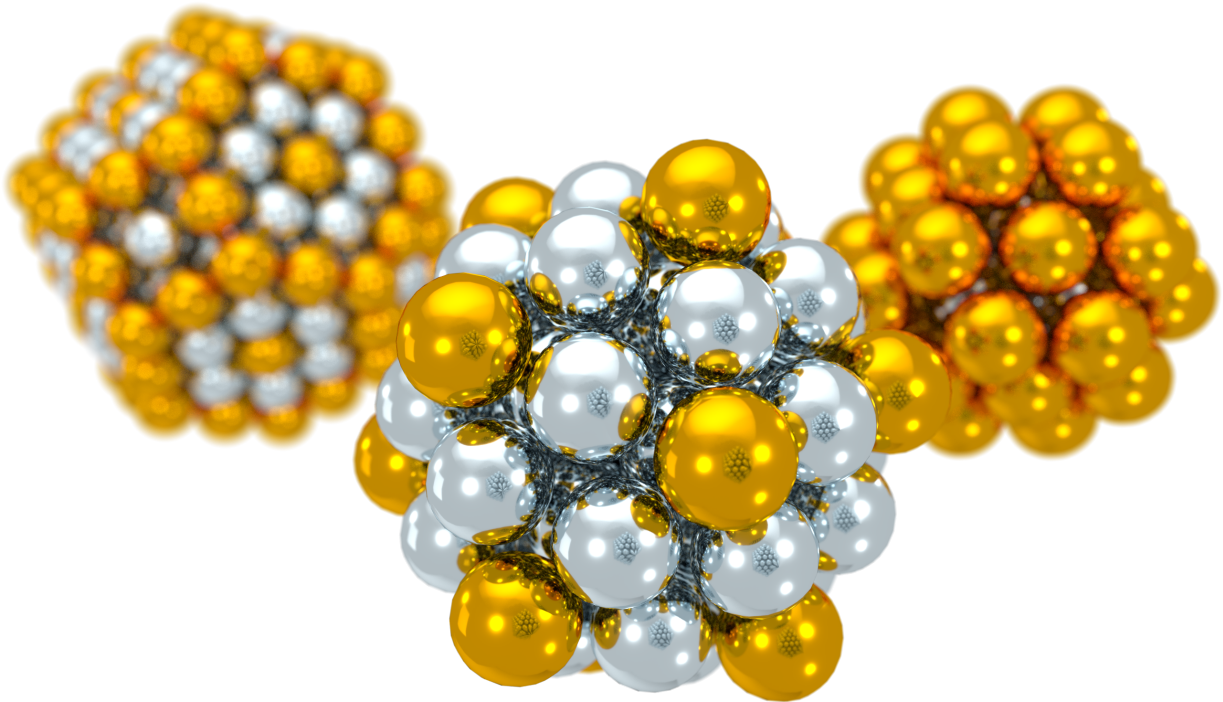




CHALMERS
UNIVERSITY OF TECHNOLOGY



Thermodynamics and Optical Response of Palladium-Gold Nanoparticles

Master's thesis in Applied Physics

MAGNUS RAHM

MASTER'S THESIS 2016

Thermodynamics and Optical Response of Palladium-Gold Nanoparticles

MAGNUS RAHM



CHALMERS
UNIVERSITY OF TECHNOLOGY

Department of Physics
Division of Materials and Surface Theory
CHALMERS UNIVERSITY OF TECHNOLOGY
Gothenburg, Sweden 2016

Thermodynamics and Optical Response of Palladium-Gold Nanoparticles
MAGNUS RAHM

© MAGNUS RAHM, 2016.

Supervisor and examiner: Paul Erhart, Department of Physics
Supervisor: Mikael Kuisma, Department of Physics

Master's Thesis 2016
Department of Physics
Division of Materials and Surface Theory
Chalmers University of Technology
SE-412 96 Gothenburg
Telephone +46 31 772 1000

Cover: Rendition of three Pd-Au nanoparticles studied in the thesis, $\text{Au}_{13}\text{Pd}_{42}$ icosahedron (front), $\text{Au}_{74}\text{Pd}_{127}$ regular truncated octahedron (left) and $\text{Au}_{32}\text{Pd}_6$ regular truncated octehadron (right).

Typeset in L^AT_EX
Printed by Chalmers Reproservice
Gothenburg, Sweden 2016

Thermodynamics and Optical Response of Palladium-Gold Nanoparticles
MAGNUS RAHM
Department of Physics
Chalmers University of Technology

Abstract

Alloyed nanoparticles of palladium (Pd) and gold (Au) are promising candidates for hydrogen sensing in e.g., cars powered by fuel cells. Specifically, the plasmonic response of Pd-Au nanoparticles changes upon absorption of hydrogen, enabling quantitative measurement of the hydrogen partial pressure. The optical properties of alloyed nanoparticles are not only dependent on the concentration of the respective element, but also on the atomic ordering. This thesis presents atomistic simulations as well as first-principles calculations on Pd-Au nanoparticles, where the former aim at elucidating the thermodynamics, and the latter were conducted to investigate the optical properties of representative particles. A novel algorithm for determination of optical nanoparticle shapes, based on Monte Carlo simulations, is also presented. The atomistic simulations show that Au tends to segregate to the surface of the nanoparticle, especially at corner and edge sites, while the subsurface layer exhibits a Pd excess. The first-principles calculations, specifically density functional theory (DFT) and time-dependent density functional theory (TDDFT), show that the electronic oscillations occur almost exclusively on the surface of the particles, while the interior atoms play an important role in screening of the optical response. The calculations do not, however, reveal any distinct plasmonic peak in the optical absorption spectra.

Keywords: palladium, Pd, gold, Au, LSPR, TDDFT, plasmonics, optical absorption, nanoparticles, nanoalloys

Acknowledgements

I would like to express my sincere gratitude to my supervisor and examiner Paul Erhart. Your passion for sharing your knowledge in physics is truly inspiring and this thesis would not have been even remotely possible without you. I am also very grateful to my supervisor Mikael Kuisma. Your help has been crucial in many parts of this thesis. The people at the division of Materials and Surface Theory also deserve to be mentioned, for good advice and guidance in many respects, big and small, but also for creating such a welcoming atmosphere. Finally, I would like to thank my family and friends. Without your love and support, none of this would have been possible.

Magnus Rahm, Gothenburg, June 2016

Contents

List of Figures	xi
List of Tables	xiii
1 Introduction	1
2 Localized surface plasmon resonance	3
2.1 Classical approach	3
2.1.1 The free electron model	3
2.1.2 Homogeneous nanoparticles	5
2.1.3 The influence of shape	7
2.1.4 Alloyed nanoparticles	7
2.2 Quantum mechanical approach	8
2.2.1 Single-particle and collective excitations	9
2.2.2 Identifying the plasmon resonance	9
3 Computational methods	11
3.1 Connection between statistical mechanics and thermodynamics	11
3.1.1 The microcanonical ensemble	12
3.1.2 The canonical ensemble	13
3.1.3 The grand and semigrand canonical ensemble	14
3.1.4 The variance-constrained semigrand canonical ensemble	16
3.2 Atomistic modeling	17
3.2.1 Molecular Dynamics simulations	17
3.2.2 Monte Carlo integration	18
3.2.3 Atomistic modeling of alloys	18
3.3 Electronic structure modeling	19
3.3.1 Density functional theory	19
3.3.2 Time-dependent density functional theory	21
3.3.3 The projector augmented wave method	22
3.3.4 Time-propagation and optical absorption	23
4 Thermodynamics of Pd-Au alloys	25
4.1 Computational details	25
4.2 Bulk properties	26
4.2.1 Searching for ordered configurations	28
4.2.2 Acceptance probability and temperature	29

4.3	Surface properties	29
4.3.1	Surface energies	30
4.3.2	Surface segregation and atomic ordering	32
4.4	Nanoparticle shapes	33
4.4.1	The truncated octahedron	33
4.4.2	The icosahedron	35
4.4.3	Icosahedra versus regular truncated octahedra	36
4.5	An algorithm for the determination of optimal particle shapes	38
4.5.1	Computational procedure	38
4.5.2	Results	39
4.6	Pd-Au nanoparticles	42
4.6.1	Annealing	43
4.6.2	Verification of the potential	44
4.7	Summary	45
5	Optical response of Pd-Au nanoparticles	47
5.1	Electronic structure in bulk	47
5.1.1	Lattice parameter	48
5.2	Computational approach to nanoparticles	48
5.3	The 55 atom icosahedron	50
5.4	The 201 atom regular truncated octahedron	52
5.4.1	Induced density	53
5.4.2	The atomic density matrix	54
5.4.3	The plasmonicity index	56
5.5	Summary	57
6	Conclusions	59
	Bibliography	61

List of Figures

2.1	Relative permittivity of Au and Pd.	4
2.2	Absorption spectra for Au and Pd in quasistatic Mie theory.	6
2.3	Absorption spectra for ellipsoidal Au and Pd.	7
2.4	Theoretical absorption spectra close to the plasmon peak for Au, in core-shell and mixed nanoparticles.	8
3.1	General representation of the free energy landscape in an alloy with a miscibility gap.	16
4.1	Thermodynamics of bulk Pd-Au obtained with MD/MC simulations.	27
4.2	Acceptance probability in MD/MC simulations of bulk Pd-Au at different temperatures.	29
4.3	Structure of the fcc surfaces investigated in this thesis.	30
4.4	Concentration of Pd per atomic layer, for different values of $\Delta\mu$, in 25 layers thick slabs of Pd-Au.	31
4.5	Surface concentration of Pd as a function of concentration in the interior of the slab.	32
4.6	Ordered surface configurations.	33
4.7	Examples of geometrical structures studied in the thesis.	34
4.8	Shape of optimal truncated octahedron and a 201 atom regular truncated octahedron.	35
4.9	Energy landscape along linear interpolation between cuboctahedron and icosahedron.	36
4.10	Energy per atom relative to bulk energy for Pd and Au regular truncated octahedra and icosahedra, as a function of $N^{-1/3}$	37
4.11	Difference between energy per atom in regular truncated octahedra and icosahedra.	38
4.12	Snapshots from a particle growth run in the VC-SGC ensemble.	39
4.13	Energy per atom for structures as obtained with the particle growth method in the VC-SGC ensemble in an fcc lattice.	40
4.14	Energy per atom for icosahedral structures as obtained with the particle growth method in the VC-SGC ensemble.	41
4.15	Snapshot from particle growth run with Pd in an icosahedral lattice.	41
4.16	Chemical potential difference versus concentration at for regular truncated octahedra and icosahedra.	42
4.17	Chemical potential difference versus concentration for 38 atom regular truncated octahedron and 55 atom icosahedron.	43

4.18	Average concentration at each site in regular truncated octahedra of different sizes.	44
4.19	Trajectories from annealing in the semigrand canonical ensemble. . .	45
4.20	Ordered structures found by annealing 201 atom regular truncated octahedra.	46
4.21	Potential energy of mixing for 55 atom icosahedron and 201 atom regular truncated octahedron as obtained with the EAM potential and with DFT.	46
5.1	Band structure of Pd and Au in bulk, and corresponding density of states.	48
5.2	Density of states of Au and Pd in bulk, relative to the Fermi level, for different lattice parameters, calculated with the GLLBSC functional. . .	49
5.3	Density of states close to the Fermi level in icosahedral Pd ₅₅ and Au ₅₅ , as obtained with LCAO and grid-based calculations.	50
5.4	Density of states for 55 atom icosahedra with different concentrations, representing ordered as well as randomized elemental distributions. . .	51
5.5	Absorption spectra for 55 atom icosahedra.	51
5.6	Density of states for 201 atom regular truncated octahedra with different concentrations, representing ordered as well as randomized configurations.	52
5.7	Absorption spectra for 201 atom regular truncated octahedra.	53
5.8	Imaginary part of Fourier transform of induced density in Pd ₂₀₁ and Au ₂₀₁ (RTO) at frequencies corresponding to 2, 4, 6 and 8 eV.	54
5.9	Imaginary part of Fourier transform of atomic transition density matrix elements for Au ₂₀₁ (RTO).	55
5.10	Imaginary part of Fourier transform of atomic density matrix elements for 201 atoms RTO, summed over atoms according to the color scheme depicted in the inset.	56
5.11	Plasmonicity index for Au ₂₀₁ and Pd ₂₀₁ RTO.	57

List of Tables

3.1	Ensembles used or described in the thesis.	17
4.1	Bulk properties at 0K as obtained with EAM potential, with comparison to experiment.	26
4.2	Surface energies for Au and Pd, obtained with EAM potential, and compared to experimental values.	30

1

Introduction

In the last decades, nanoparticles have found their way into a multitude of different applications. As the particle dimensions shrink, properties that are non-existent on the macroscopic scale start to emerge. A well-known representative of this phenomenon can be observed by shining light on metallic nanoparticles. Gold is then no longer golden, but could in principle take on any color, depending on the size, shape and composition of the nanoparticles, or their surrounding medium. The reason for the change in color is that the electron cloud of the particle oscillates in response to the light, and at the resonance frequency this leads to a maximum in absorption and scattering. The resonance is referred to as localized surface plasmon resonance (LSPR). Its dependency on size, shape, composition and surrounding medium opens up a pathway to fine-tune the nanoparticles to specific applications. To do so, one has to understand the influence of the different parameters. Many insights can be acquired from classical electrodynamics, using experimentally measured dielectric functions and possibly numerical calculations. For very small particles, however, a classical approach is bound to fail since quantum mechanical effects will inevitably appear. Further, in nanoparticles that contain more than one species of atoms, a classical approach will not be able to resolve the effects that may derive from ordering of the atoms inside the nanoparticle. To overcome these limitations, first principles quantum mechanical computations may be used. Specifically, time-dependent density functional theory (TDDFT) is an outstanding candidate for describing LSPR from a fundamental, electronic point of view.

This thesis is devoted to computations of plasmonic properties of alloyed nanoparticles of palladium (Pd) and gold (Au). Pd-Au nanoparticles are interesting as candidates for hydrogen sensing in for instance cars powered with fuel cells. In short, these particles absorb hydrogen, and thereby their plasmonic properties change [1, 2]. A hydrogen leakage may then be detected from, for example, a shift in the LSPR frequency, so that catastrophic explosions can be avoided.

The computational approach in this thesis is twofold, with one part describing the thermodynamics of Pd-Au nanoparticles using classical simulations, and the other using TDDFT in an attempt to elucidate the plasmonic properties. The aim is to determine how the reduction in size affects the thermodynamic and structural properties of Pd-Au nanoparticles, and eventually the impact of these factors on plasmonic properties. The long-term goal is to use this knowledge for tailoring optimal Pd-Au hydrogen sensors.

The thesis is structured as follows. Chapter 2 describes LSPR from both a classical and quantum mechanical perspective, attempting to bridge the conceptual gap between the two, as well as paving the way for the analysis of TDDFT results.

1. Introduction

Chapter 3 describes the computational methods used in the thesis, as well as the underlying physics. Chapter 4 presents the results from the classical simulations, aiming for a description of the thermodynamics of Pd-Au nanoparticles. TDDFT results and optical absorption spectra are in the focus of Chapter 5, and the thesis is wrapped up in Chapter 6, summarizing the main conclusions and providing an outlook.

2

Localized surface plasmon resonance

The property of small particles to absorb and scatter light in a fashion different from bulk materials has been known for a long time [3]. This is not surprising since localized surface plasmon resonance (LSPR) appears as a solution to Maxwell's equations in very simple geometries. Describing LSPR on the electronic scale is however more tedious, and much is still not fully understood. This chapter gives a brief review of the classical description of LSPR, as well as some considerations on how to approach the phenomenon quantum mechanically.

2.1 Classical approach

LSPR can in essence be derived by studying a metallic sphere in an oscillating electric field. The behavior of such a system is closely related to the movement of the electrons in the sphere. The dielectric function ϵ is a material property quantifying the response of the electrons under the influence of an electric field, and it is consequently necessary to understand the dielectric function in order to understand LSPR. Hence, this section begins with a glance at the simplest model of the electronic properties of a metal, the free electron model.

2.1.1 The free electron model

The classical equation of motion for an electron with charge $-e$ and mass m_e subject to an electric field \mathbf{E} and damped in proportion to its velocity, is

$$m_e \ddot{\mathbf{x}} + \gamma m_e \dot{\mathbf{x}} = -e \mathbf{E}. \quad (2.1)$$

If an harmonically oscillating electric field is assumed, $\mathbf{E} = \mathbf{E}_0 e^{-i\omega t}$, the solution is given by

$$\mathbf{x} = \frac{e \mathbf{E}}{m_e \omega^2 + i \gamma m_e \omega}. \quad (2.2)$$

The displacement of the charge gives rise to a dipole moment,

$$\mathbf{p} = -e \mathbf{x} = -\frac{e^2 \mathbf{E}}{m_e \omega^2 + i \gamma m_e \omega}. \quad (2.3)$$

If the density of electrons is n , the polarization field is

$$\mathbf{P} = -\frac{ne^2}{m_e \omega^2 + i \gamma m_e \omega} \mathbf{E}. \quad (2.4)$$

2. Localized surface plasmon resonance

The displacement field \mathbf{D} , famous from Maxwell's macroscopic equations, is thus given by

$$\mathbf{D} = \epsilon_0 \mathbf{E} + \mathbf{P} = \epsilon_0 \left(1 - \frac{ne^2}{(m_e \omega^2 + i\gamma m_e \omega)} \right) \mathbf{E} \quad (2.5)$$

where ϵ_0 is the permittivity of vacuum. The relative permittivity in the free electron model is thus

$$\epsilon_r = 1 - \frac{ne^2}{(m_e \omega^2 + i\gamma m_e \omega)} = 1 - \frac{\omega_p^2}{\omega^2 + i\gamma\omega} = 1 - \frac{\omega_p^2}{\omega^2 + \gamma^2} + i \left[\frac{\omega_p^2 \gamma}{\omega(\omega^2 + \gamma^2)} \right] \quad (2.6)$$

where the so-called plasma frequency

$$\omega_p^2 = \frac{ne^2}{m_e \epsilon_0} \quad (2.7)$$

has been introduced.

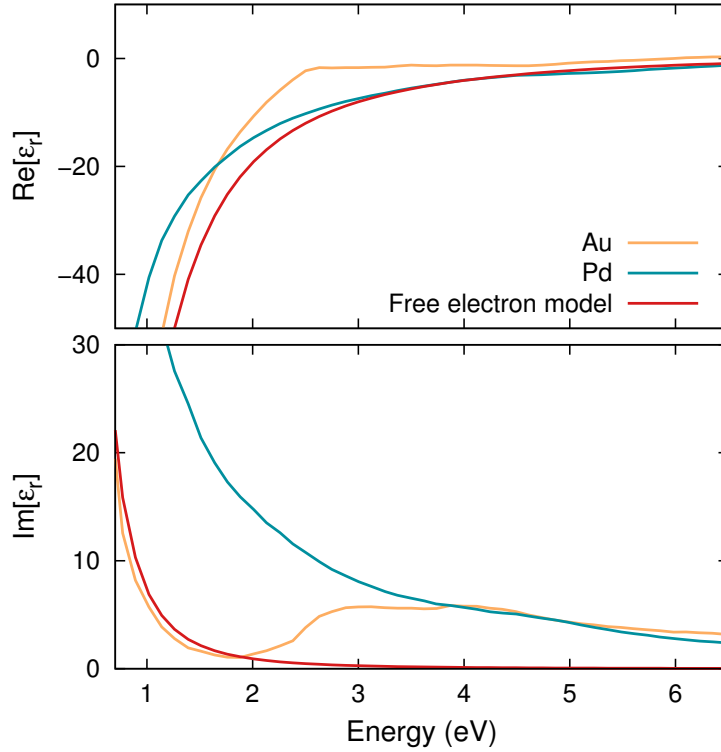


Figure 2.1: The real (top) and imaginary (bottom) parts of the relative permittivity of Au and Pd. Experimental data taken from Ref. 4, the free electron model with an electron density of $5.9 \cdot 10^{22}$ electrons/cm³, resulting in $\omega_p \approx 1.4 \cdot 10^{16}$ s⁻¹, and damping $\gamma = 0.01\omega_p$.

It is interesting to see how this model compares to experiment. Figure 2.1 shows experimental data for the relative permittivity, in comparison with the prediction provided by Eq. (2.6). Note that the agreement is fairly good for the real part. For the imaginary part there is only good agreement with Au in the low frequency regime. For higher frequencies, the free electron model predicts the imaginary part to go to zero, i.e. the damping to become negligible. Experimental data, however,

shows an increase in the imaginary part for frequencies above 2-3 eV. This can be understood by studying the electronic structure of Au. Au can in a simple picture be described as a system of 68 core electrons and 11 valence electrons. Ten of the valence electrons fill the 5*d* shell. In bulk Au the levels hybridize, forming a *d*-band. The remaining valence electron is put in the 6*s* level, which in bulk hybridizes with the 6*p* level, forming an *sp*-band. In bulk, only the electrons in the *sp*-band should be regarded as free. It turns out that the distance between the *d*-band edge and the Fermi level is roughly 2 eV [5]. The increase of the imaginary part of the dielectric function is thus a manifestation of the onset of excitations of electrons from the *d*-band to the *sp*-band. The picture of Au as a sea of free electrons thus breaks down for frequencies above 2 eV. Further, Pd is seen to have a larger imaginary part than Au for all frequencies. Pd being an element in the group to the left of Au in the periodic table, has no valence *s* electrons. Rather the highest level is 4*d*, which is filled with 10 electrons. The notion of Pd as a sea of free electrons is thus questionable, regardless of frequency.

2.1.2 Homogeneous nanoparticles

Having discussed the general features of the dielectric functions of Au and Pd, it is time to see how they relate to the optical response of nanoparticles of these metals. Consider a homogeneous spherical body with radius a and dielectric function ϵ_s embedded in a material with dielectric function ϵ_m (possibly vacuum in which case $\epsilon_m = 1$), subject to an external electric field $\mathbf{E} = E_0 \hat{z}$. The resulting field is given by solving the Laplace equation

$$\nabla^2 \phi = 0 \quad (2.8)$$

and recovering the field via $\mathbf{E}_{\text{tot}} = -\nabla \phi$. By making use of the azimuthal symmetry and applying proper boundary conditions, the solution can be shown to be [6]

$$\phi_{\text{in}} = \frac{-3\epsilon_m}{\epsilon_s + 2\epsilon_m} E_0 z \quad (2.9)$$

$$\phi_{\text{out}} = -E_0 z + \frac{\epsilon_s - \epsilon_m}{\epsilon_s + 2\epsilon_m} E_0 a^3 \frac{\cos \theta}{r^2} \quad (2.10)$$

for the fields inside and outside of the sphere, respectively. Notice that the latter expression looks exactly like the applied field (the first term) with a superimposed field from a dipole (the second term). This can be interpreted as the external field inducing a collective displacement of the electrons in the sphere, effectively turning the particle into an oscillating dipole. With some rearrangement the induced dipole can be defined as

$$\mathbf{p} = 4\pi\epsilon_0\epsilon_m a^3 \frac{\epsilon_s - \epsilon_m}{\epsilon_s + 2\epsilon_m} \mathbf{E} = \epsilon_0\epsilon_m \alpha \mathbf{E}, \quad (2.11)$$

where the polarizability was defined,

$$\alpha = 4\pi a^3 \frac{\epsilon_s - \epsilon_m}{\epsilon_s + 2\epsilon_m}. \quad (2.12)$$

It should be remembered that the dielectric function is dependent on the frequency ω of the field. The above reasoning thus holds only if the field varies so slowly that

the external field can be regarded as constant over the whole particle at any given instant of time, i.e. that the wavelength λ is much longer than the radius a . This is referred to as the quasistatic approximation.

The induced field is associated with optical absorption. An analysis of the Poynting vector leads to an expression for the cross-section of absorption [6]

$$C_{\text{abs}} = \frac{2\pi}{\lambda} \text{Im} \alpha = \frac{8\pi^2 a^3}{\lambda} \text{Im} \left[\frac{\epsilon_s - \epsilon_m}{\epsilon_s + 2\epsilon_m} \right]. \quad (2.13)$$

The absorption is thus highly dependent on the dielectric function of the surrounding medium. In first-principles computations it would usually be vacuum, in which case $\epsilon_m = 1$ and $2\pi/\lambda = \omega/c$, and the absorption simplifies to

$$C_{\text{abs, vacuum}} = \frac{4\pi a^3 \omega}{c} \text{Im} \left[\frac{\epsilon_s - 1}{\epsilon_s + 2} \right]. \quad (2.14)$$

The above expression allows for a resonance at

$$\text{Re} \epsilon_s(\omega) = -2, \quad (2.15)$$

provided that $\text{Im} \epsilon_s(\omega)$ is small. This is referred to as localized surface plasmon resonance (LSPR).

Figure 2.2 shows the absorption spectra for Au and Pd obtained with Eq. (2.14). At 2.5 eV, where $\text{Re} \epsilon_{\text{Au}} = -2$, there is a peak in the Au spectrum. From Eq. (2.14) it is clear that the prominence of the resonance will be highly dependent on the imaginary part of ϵ_s . Indeed, if $\text{Im} \epsilon_s = 0$ when $\text{Re} \epsilon_s = -2$, the absorption would diverge. Thus, the fact that the plasmon peak for Au is located exactly where transitions from the d -band start to kick in, means that the peak is embedded in a part of the spectrum where absorption is also due to excitations of d electrons. For Pd, the resonant condition Eq. (2.15) is fulfilled at approximately 5.7 eV, but there the imaginary part of ϵ is too dominant for a peak to appear.

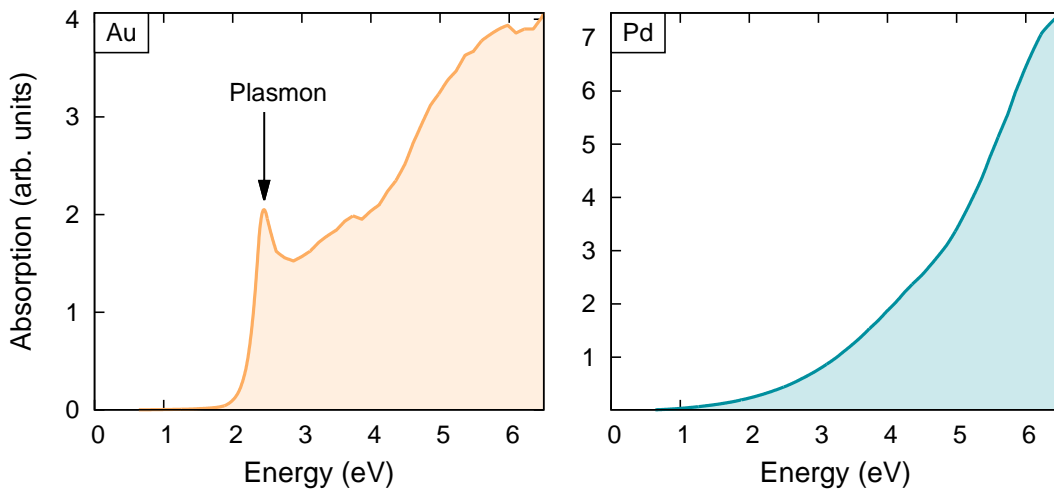


Figure 2.2: Absorption spectra for Au (left) and Pd (right) as obtained with Eq. (2.14). Dielectric functions obtained from Ref. 4.

It should be mentioned that a spectrum obtained in an experimental measurement typically does not only include absorption but also scattering. The latter can be derived analytically in the same manner as was done in the case of absorption. Here, scattering was excluded, since the scaling is different. While the absorption cross section was seen to scale with the volume of the particle, the scattering scales with the volume squared [6], and is thus negligible for the very small particles that can be handled with first principles computations.

2.1.3 The influence of shape

In the previous section, the absorption spectrum was derived for a spherical particle in a quasistatic field. For more complicated shapes, one would typically have to employ a numerical approach. An interesting exception, for which analytic solutions are available, are ellipsoids [7]. Figure 2.3 shows absorption spectra in the special case of an oblate, i.e. an ellipsoid where the two longer axes are equal. With the field polarized along these longer axes, the plasmon is redshifted. For Au, this means that the plasmon is redshifted away from the d -band, whence the intensity of the plasmon peak increases. For Pd, the redshift implies that the plasmon peak enters the visible spectrum (where there is also experimental data for the dielectric function).

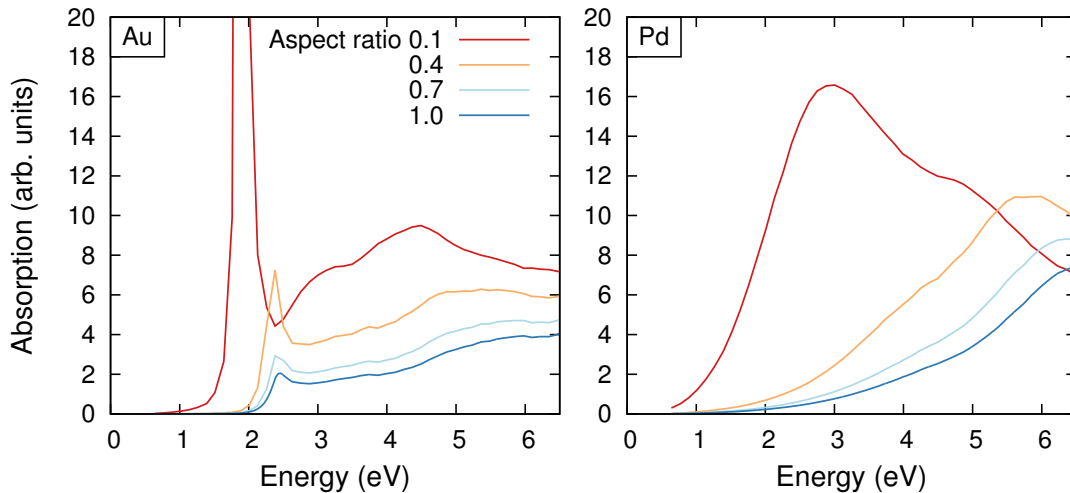


Figure 2.3: Absorption spectra for ellipsoidal Au (left) and Pd (right), with aspect ratios ranging between 0.1 and 1.0. Dielectric functions obtained from Ref. 4.

2.1.4 Alloyed nanoparticles

For an alloyed particle, the situation is more complex. The dielectric function would then have different forms depending on how the atoms mix. If the system is segregated so that there is a spherical core of one species covered by a spherical shell of another, there still exists an analytic solution [7]:

$$C_{\text{abs, vacuum}} = \frac{4\pi a^3 \omega}{c} \text{Im} \left[\frac{(\epsilon_s - 1)(\epsilon_c + 2\epsilon_s) + g(\epsilon_c - \epsilon_s)(\epsilon_m + 2\epsilon_s)}{(\epsilon_s + 2)(\epsilon_c + 2\epsilon_s) + g(2\epsilon_s - 2)(\epsilon_c - \epsilon_s)} \right] \quad (2.16)$$

where ϵ_c and ϵ_s are the dielectric functions of core and shell, respectively, and g is the volume fraction of the core element. Figure 2.4 shows the spectra thus obtained with $g = 0.05$ and $g = 0.95$ with Pd in core and shell respectively, i.e. with 5 vol-% of Pd put in either the core or the shell. Note that the impact on the spectrum is somewhat larger with Pd on the surface, as compared to Pd in the core. This observation is consistent with the common perception of LSPR as a surface phenomenon. Figure 2.16 also contains the absorption spectrum obtained with Eq. (2.14), by mixing the dielectric functions according to

$$\epsilon_{\text{mix}}(\omega) = 0.95\epsilon_{\text{Au}} + 0.05\epsilon_{\text{Pd}}. \quad (2.17)$$

It is perhaps somewhat surprising that this way of mixing the dielectric functions affects the absorption spectrum more than putting all Pd on the surface. It is hard to know, however, how this way of mixing the dielectric functions relates to the situation in a real Pd-Au alloy.

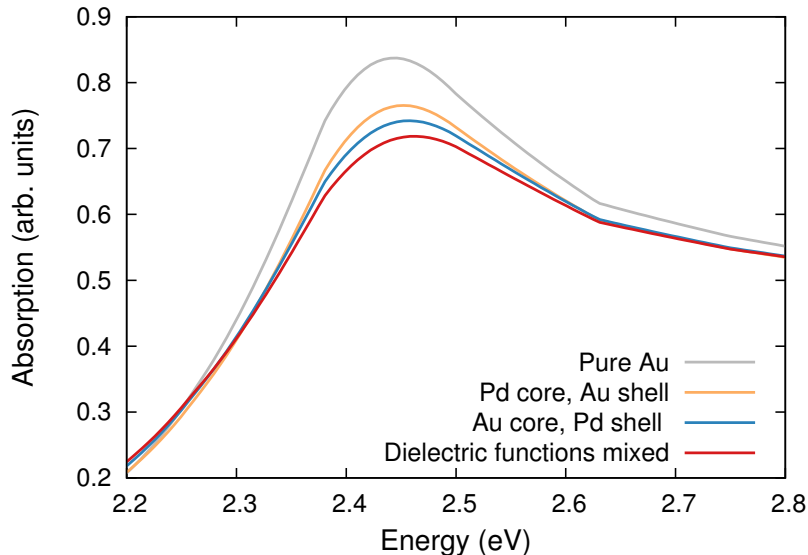


Figure 2.4: Absorption spectra close to the plasmon peak for Au, as obtained with Eq. (2.16). In the core-shell particles, 5 vol-% Pd was added. The red curve was obtained with a homogeneous sphere, with the dielectric function mixed with 95 % Au and 5 % Pd. Dielectric functions obtained from Ref. 4.

2.2 Quantum mechanical approach

While the results of the preceding section are attractive due to their simplicity, it is important to be aware of their limited range of validity. The results were derived in the quasistatic limit, where the particle is assumed to be much smaller than the wavelength. With a larger particle, this condition is of course violated. Nevertheless, large particles can still be handled analytically with more sophisticated methods, and a size dependency will appear in the expression for the plasmon peak. In the other end of the spectrum, however, there is a more severe limitation. For very small

particles, the dielectric function is no longer well-defined and quantum mechanical effects appear.

2.2.1 Single-particle and collective excitations

Consider an electron in a state $|\phi_i\rangle$ with energy $\hbar\omega_i$, under influence of an electromagnetic field with frequency ω . Quantum mechanical intuition tells that it should be possible to excite the electron to a state $|\phi_j\rangle$ with energy $\hbar\omega_j$ provided that the energies match, i.e. that $\omega = \omega_j - \omega_i \equiv \omega_{ji}$. This is not the full story, since energy is not the only conserved quantity. By first-order time-dependent perturbation theory, one can show [8] that the cross-section for the transition, with a field polarized along the z axis, is

$$C_{\text{abs}} = 4\pi^2\alpha \sum_j \omega_{ji} |\langle \phi_j | z | \phi_i \rangle|^2 \delta(\omega - \omega_{ji}) \quad (2.18)$$

where α is the fine structure constant.

Consider now a system of many electrons, where each state $|\phi_i\rangle$ is occupied by f_i electrons. Inspired by Eq. (2.18) it is tempting to write the cross section as

$$C_{\text{abs}} = 4\pi^2\alpha \sum_{i,j} \omega_{ji} |\langle \phi_j | x | \phi_i \rangle|^2 \delta(\omega - \omega_{ji}) (1 - f_i) f_j. \quad (2.19)$$

The occupation numbers factor $(1 - f_i)f_j$ makes sure that excitations are only allowed from an occupied to a non-occupied state. Equation (2.19) can quite easily be evaluated with a ground state DFT calculation, using Kohn-Sham states for $|\phi_i\rangle$ and $|\phi_j\rangle$ (see Chapter 3). As it turns out, however, it does not reproduce the absorption in a real system. The reason is that no interaction between the electrons is accounted for in Eq. (2.19) [9]. With interaction, the levels may hybridize such that a new transition with eigenenergy $\hbar\omega$ is collectively built up by many quasiparticle transitions that all have $\omega_{ji} < \omega$. Such an excitation is called a plasmon.

In a quasiparticle description, there will thus be two main categories of excitations, those of single-particle character, and collective ones. Any absorption spectrum will be a mixture of the two, and the distinction is not always clear. For small systems, single particle excitations tend to dominate. As the system size grows, collective excitations become increasingly important, and may start to dominate the spectrum. Really large systems are intractable with today's first principles computational methods, and a way to discern plasmonic excitations in a jungle of single-particle excitations is therefore sought after.

2.2.2 Identifying the plasmon resonance

Several methods to identify plasmonic excitations from a TDDFT calculation have been proposed. Bernadotte *et al.* [9] introduced a parameter λ that scales the interaction between the electrons, and did many calculations with λ ranging from 0 to 1 corresponding to no interaction and full interaction, respectively. The energies of plasmonic excitations were seen to increase significantly when the interaction was turned on, as opposed to single-particle excitations that had roughly the same energy for all values of λ . This approach made the plasmon identification straightforward, but the method requires multiple expensive calculations on artificial systems.

Another approach was proposed by Ma *et al.* [10]. In first-order perturbation theory, a time-dependent wavefunction for a single particle may be expressed as

$$\psi_i(t) \approx e^{-i\omega_i t} \phi_i + C_{j,i}(t) e^{-i\omega_j t} = e^{-i\omega_i t} \left(\phi_i + C_{j,i}(t) e^{-i(\omega_j - \omega_i)t} \phi_j \right). \quad (2.20)$$

They were able to show that the expansion coefficients $C_{j,i}(t)$ are much more rapidly varying for plasmonic excitations than for single-particle excitations. The Fourier transform of $C_{j,i}$ thus reveals the nature of the excitation. The drawback is that the method requires storage of lots of data that is usually not saved in a TDDFT calculation, as well as prior knowledge of the position of the plasmon peak (or multiple calculations for different energies).

A simpler measure, based on data that is usually available from a TDDFT calculation, was recently published by Bursi *et al.* [11]. It is based on observations on how the induced potential is supposed to behave for plasmonic and non-plasmonic excitations, and reads

$$\tilde{\eta}_P(\omega) = \frac{\int |\int n(\mathbf{r}', \omega) |\mathbf{r}' - \mathbf{r}|^{-1} d^3 r'|^2 d^3 r}{\int |n(\mathbf{r}, \omega)|^2 d^3 r} \quad (2.21)$$

where $n(\mathbf{r}, \omega)$ is the Fourier transformed induced charge density, or specifically its imaginary part. The authors proposed that the value of $\tilde{\eta}_P(\omega)$ is a measure of the plasmonic content of a peak at the frequency ω . Note that the inner integral in the numerator is a convolution between the functions $n(\mathbf{r})$ and $1/|\mathbf{r}|$. It can therefore be advantageous to write $\tilde{\eta}_P$ in terms of Fourier transforms,

$$\tilde{\eta}_P(\omega) = \frac{\int |4\pi \mathcal{F}^{-1} \{ \hat{n}(\mathbf{k}, \omega) k^{-2} \}|^2 d^3 r}{\int |n(\mathbf{r}, \omega)|^2 d^3 r} \quad (2.22)$$

where \mathcal{F}^{-1} denotes inverse Fourier transform and $\hat{n}(\mathbf{k}, \omega)$ is the induced density Fourier transformed into reciprocal space with wave number \mathbf{k} . Since the Fourier transform of $1/|\mathbf{r}|$ is just $4\pi/k^2$, the quantity $\tilde{\eta}_P$ is essentially a low-pass filter, assigning more weight to oscillations occurring on a longer spatial scale. The usefulness of this so-called plasmonicity index is still to be assessed, but out of the approaches described here, it is the most readily available, and it has therefore been implemented in this thesis.

3

Computational methods

This chapter aims at giving a general introduction to the computational methods used in this thesis. The methods can be grouped into classical and quantum mechanical. The former are based on statistical mechanics and its connection to thermodynamics, and the first part of this chapter is therefore devoted to a review of this subject, to a large extent inspired by Ref. 12. The second part gives a description of the classical methods, specifically Molecular Dynamics simulations and Monte Carlo integration. The third and last part describes density functional theory and time-dependent density functional theory, which are both used in this thesis for computations of the optical response of Pd-Au nanoparticles.

3.1 Connection between statistical mechanics and thermodynamics

Consider a system with N identical particles in a volume V . The state of the system can be described by specifying the positions \mathbf{r} as well as the momenta \mathbf{p} of all N particles in all 3 dimensions. The state can thus be characterized by

$$(\mathbf{r}, \mathbf{p}) = (r_1, r_2, \dots, r_{3N}, p_1, p_2, \dots, p_{3N}) \quad (3.1)$$

and it has energy E , comprising potential as well as kinetic energy. Of course, there are generally many different states (\mathbf{r}, \mathbf{p}) with N particles in the volume V that have the same energy E . We say that there are different microstates corresponding to the same macrostate (N, V, E) .

Now, consider two such systems in thermal contact with each other but otherwise isolated. By thermal contact, we mean that they can exchange energy. In equilibrium, they will therefore be equally willing to give up energy to each other, a property we know as temperature. We denote the energies of the systems E_1 and E_2 , respectively, and the total energy, given by $E_0 = E_1 + E_2$, is fixed since the systems are isolated from the outside world. How is the total energy distributed between E_1 and E_2 in equilibrium? Guided by the second law of thermodynamics, we can assume that the distribution will be such that the number of microstates, denoted Ω_0 , is maximized. The total number of microstates is the product of the number of microstates in system 1 and system 2,

$$\Omega_0 = \Omega_1(E_1)\Omega_2(E_2) = \Omega_1(E_1)\Omega_2(E_0 - E_1) \quad (3.2)$$

If we denote \bar{E}_1 and \bar{E}_2 as the energies leading to maximized Ω_0 , we have

$$\left. \frac{d\Omega_0}{dE_1} \right|_{\bar{E}_1} = 0, \quad (3.3)$$

or if we rewrite the left hand side using Eq. (3.2),

$$\left. \frac{d\Omega_0}{dE_1} \right|_{\bar{E}_1} = \left. \frac{\partial \Omega_1(E_1)}{\partial E_1} \right|_{\bar{E}_1} \Omega_2(\bar{E}_2) + \Omega_1(\bar{E}_1) \left. \frac{\partial \Omega_2(E_2)}{\partial E_2} \right|_{\bar{E}_2} \frac{\partial E_2}{\partial E_1} = 0. \quad (3.4)$$

Since $E_2 = E_0 - E_1$ we have $\partial E_2 / \partial E_1 = -1$ and we can rewrite the above equation,

$$\left(\frac{\partial \ln \Omega_1(E_1)}{\partial E_1} \right)_{\bar{E}_1} = \left(\frac{\partial \ln \Omega_2(E_2)}{\partial E_2} \right)_{\bar{E}_2}. \quad (3.5)$$

Hence, we have that in thermal equilibrium, the quantity

$$\frac{\partial \ln \Omega(E)}{\partial E} \quad (3.6)$$

is the same in both systems. To proceed, we recall that in thermodynamics, temperature can be defined by

$$\frac{1}{T} = \left(\frac{\partial S}{\partial E} \right)_{N,V}. \quad (3.7)$$

Comparing (3.6) and (3.7), it is natural to write

$$S = k_B \ln \Omega \quad (3.8)$$

where the constant of proportionality k_B is referred to as Boltzmann's constant. Equation (3.8) establishes a connection between thermodynamics and statistical mechanics by connecting the macroscopic quantity S and the microscopic quantity Ω .

3.1.1 The microcanonical ensemble

A completely isolated system is characterized by constant number of particles N , constant volume V and constant energy E . The set of all possible microstates having the same N , V and E is called the microcanonical ensemble. In such a system the entropy $S = k_B \ln \Omega$ will be maximized. For reasons that will become clear later, we can introduce the quantity

$$\rho(s) = \begin{cases} 1 & \text{if } s \text{ is a microstate with } (N, V, E), \\ 0 & \text{otherwise,} \end{cases} \quad (3.9)$$

and we can write the number of accessible microstates as

$$\Omega = \sum_s \rho(s) \quad (3.10)$$

where the sum runs over all microstates s .

Thermodynamically, the entropy can be related to the constant variables N , V and E by the thermodynamic identity

$$dE = TdS - pdV + \mu dN \quad \Rightarrow \quad dS = \frac{1}{T}dE + \frac{p}{T}dV - \frac{\mu}{T}dN. \quad (3.11)$$

3.1.2 The canonical ensemble

Even though the microcanonical ensemble serves a purpose in understanding statistical mechanics, it is generally not realized in experiments. A much more common situation is that the system under investigation is in thermal contact with the surrounding environment so that its energy may vary. If the surrounding is treated as a reservoir, so that its temperature stays the same no matter how much energy it receives or gives away, we obtain the canonical ensemble, which consequently has fixed (N, V, T) . We may denote the energy of the system E and the energy of the reservoir E_r , and we have $E_0 = E + E_r$ fixed. Note that, in contrast to the microcanonical ensemble, we have T fixed while the energy E may vary.

A macrostate is now characterized by the maximum entropy in the system and reservoir together. The total number of microstates is given by the product of the number of microstates in the system and in the reservoir,

$$S_{\text{tot}} = k_B \ln \Omega_s \Omega_r = k_B \ln \Omega_s + k_B \ln \Omega_r = S_s + k_B \ln \Omega_r \quad (3.12)$$

where subscript s refers to system and r to reservoir. Since E should be small compared to E_0 we can Taylor expand $\ln \Omega_r$ around E_0 ,

$$\ln \Omega_r(E_0 - E) \approx \ln \Omega_r(E_0) + \left(\frac{\partial \ln \Omega_r}{\partial E'} \right)_{E'=E_0} (E_r - E_0) \approx \text{const.} - \frac{1}{k_B T} E, \quad (3.13)$$

which we may insert into Eq. (3.12),

$$S_{\text{tot}} = S_s - k_B \frac{1}{k_B T} E + \text{const.} \quad (3.14)$$

Maximizing the total entropy is thus the same as minimizing

$$F = E - TS \quad (3.15)$$

which is known as the Helmholtz free energy (the subscript s was dropped here). The free energy is convenient since it does not refer to any quantity related to the reservoir.

The probability of finding the system in a certain microstate is no longer the same for all microstates, because by giving up energy to the reservoir, the number of possible microstates in the reservoir may change. The probability of finding the system in a certain microstate should therefore be equal to a constant times the number of microstates in the reservoir,

$$P \propto \Omega_r(E_r) = \Omega_r(E_0 - E) \quad (3.16)$$

and by combining Eq. (3.16) and (3.13) we find

$$P = C \exp\left(-\frac{E}{k_B T}\right). \quad (3.17)$$

The constant C can be found by requiring that the probabilities sum to 1, and we have

$$P = \frac{\exp(-\beta E)}{\sum_s \exp(-\beta E)} \quad (3.18)$$

where $\beta = 1/k_{\text{B}}T$ and the sum runs over all microstates with energy E . The sum

$$\mathcal{Z} = \sum_s \exp(-\beta E) \quad (3.19)$$

is referred to as the partition function. We note that it has exactly the same form as Eq. (3.10), but now with the density

$$\rho(s) = \exp(-\beta E), \quad (3.20)$$

often referred to as the Boltzmann factor. We thus have two pairs of quantities that play equivalent roles in the microcanonical and the canonical ensemble,

$$S \leftrightarrow F \quad \text{and} \quad \Omega \leftrightarrow \mathcal{Z} \quad (3.21)$$

and we may, guided by intuition, guess that the relationship $S = k_{\text{B}} \ln \Omega$ also has an analog,

$$F = -k_{\text{B}}T \ln \mathcal{Z} \quad (3.22)$$

which indeed turns out to be true. Equation (3.22) can be regarded as the connection between thermodynamics and statistical mechanics in the canonical ensemble.

Finally, we can make a modification of the thermodynamic identity,

$$\begin{aligned} dE - d(TS) &= TdS - pdV + \mu dN - d(TS) \\ \Rightarrow d(E - TS) &= dF = -SdT - pdV + \mu dN. \end{aligned} \quad (3.23)$$

3.1.3 The grand and semigrand canonical ensemble

Up to this point, all the systems have had a fixed number of particles. We can also imagine a system that not only can exchange energy with a reservoir, but also particles. When the system and reservoir are allowed to exchange energy, they will have the same temperature in equilibrium. When particles are exchanged, the quantity that is the same in equilibrium is the chemical potential μ . The grand canonical ensemble is thus characterized by constant (μ, V, T) . The reasoning in the previous section can be applied also in this case, and for example we get

$$d(E - TS - \mu N) = d\Phi = -SdT - pdV - Nd\mu \quad (3.24)$$

where $\Phi = E - TS - \mu N$ usually is referred to as the grand potential. Furthermore, we have

$$\Phi = -k_{\text{B}}T \ln \Xi \quad (3.25)$$

where Ξ is the grand partition function, defined by

$$\Xi = \sum_s \exp(-\beta(E - N\mu)) \quad (3.26)$$

The above ensembles can easily be generalized to a system with two (or more) kinds of particles, say A and B . In the canonical ensemble we then have constant (N_A, N_B, V, T) and in the grand canonical ensemble constant (μ_A, μ_B, V, T) . We can also define an ensemble that could be regarded as intermediate between the

canonical and grand canonical. To do so, we fix the total number of particles and the difference in chemical potential between species A and B , i.e. we have constant $(N_{\text{tot}}, \Delta\mu, V, T)$. The thermodynamic identity can then be modified as in the following,

$$\begin{aligned} d(E - TS) &= -SdT - pdV + \mu_A dN_A + \mu_B dN_B \\ &= -SdT - pdV - (\mu_B - \mu_A) dN_A + \mu_B (dN_A + dN_B) \\ &= -SdT - pdV - \Delta\mu dN_A + \mu_B dN_{\text{tot}} \end{aligned} \quad (3.27)$$

and adding $d(\Delta\mu N_A)$ to both sides we end up with

$$d(E - TS + \Delta\mu N_A) = -SdT - pdV + N_A d\Delta\mu + \mu_B dN_{\text{tot}} \quad (3.28)$$

or equivalently

$$d(E - TS + N_{\text{tot}} c \Delta\mu) = -SdT - pdV + N_{\text{tot}} c d\Delta\mu + \mu_B dN_{\text{tot}} \quad (3.29)$$

where $c = N_A/N_{\text{tot}}$ is the concentration of species A . By defining a semigrand potential

$$\Psi = E - TS + N_{\text{tot}} c \Delta\mu \quad (3.30)$$

we can write

$$\Psi = -k_B T \ln \Upsilon \quad (3.31)$$

where

$$\Upsilon = \sum_s \rho(s) = \sum_s \exp(-\beta(E + N_{\text{tot}} c \Delta\mu)). \quad (3.32)$$

The sum in Eq. (3.32) runs over many states with different concentration c . To establish a thermodynamic relation between $\Delta\mu$ and the free energy, one can rewrite Eq. (3.32) in terms of an integral over all concentrations and the canonical partition function at a particular concentration [13]

$$\Upsilon(N, V, T, \Delta\mu) = \int_0^1 \mathcal{Z}(N, V, T, c) \exp(-\beta N_{\text{tot}} c \Delta\mu) dc, \quad (3.33)$$

where the dependencies of the different ensembles have been written out for clarity. Now, Eq. (3.22) can be rewritten as $Z = \exp(-\beta F)$, which inserted into Eq. (3.33) yields

$$\Upsilon(N, V, T, \Delta\mu) = \int_0^1 \exp(-\beta(F(N, V, T, c) + N_{\text{tot}} c \Delta\mu)) dc. \quad (3.34)$$

The integrand in Eq. (3.34) defines a concentration distribution in the semigrand canonical ensemble. The distribution is peaked around the average concentration $\langle c \rangle$, where the derivative consequently is zero,

$$\exp(\beta(-F(N, V, T, c) + N_{\text{tot}} c \Delta\mu)) \left(-\beta \frac{\partial F(N, V, T, c)}{\partial c} - \beta N_{\text{tot}} \Delta\mu \right) = 0 \quad (3.35)$$

so that

$$\Delta\mu = -\frac{1}{N_{\text{tot}}} \frac{\partial F}{\partial c}(N, V, T, \langle c \rangle). \quad (3.36)$$

Equation (3.36) is useful for calculating the free energy from $\Delta\mu$ and c , which are both available in atomistic simulations in the semigrand canonical ensemble.

3.1.4 The variance-constrained semigrand canonical ensemble

As will be seen in Section 3.2.2, the semigrand canonical ensemble provides means for convenient simulations of alloys. It does, however, have a main disadvantage. Consider an alloy with a miscibility gap, i.e. an alloy in which the constituents do not mix in all proportions. Fig. 3.1a shows the free energy landscape in a fictitious system of that kind, with the miscibility gap manifested by the central maximum. The corresponding $\Delta\mu$ is shown in Fig. 3.1b. Note that a single value of $\Delta\mu$ maps to multiple concentrations. By specifying $\Delta\mu$, one could therefore in principle end up at three different concentrations. In a real simulation, one therefore cannot equilibrate a concentration inside the miscibility gap. Sampling the free energy landscape inside the miscibility gap is thus impossible within the semigrand canonical ensemble.

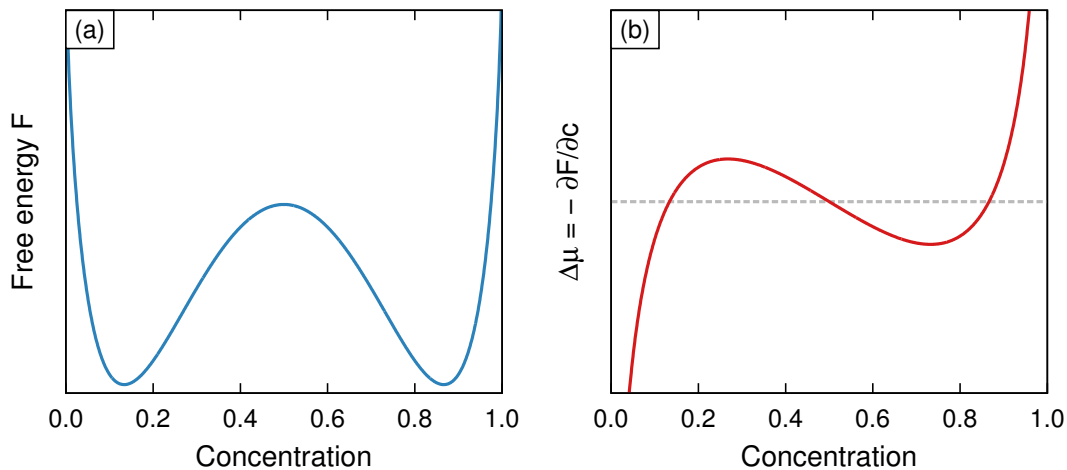


Figure 3.1: General representation of the free energy landscape in an alloy with a miscibility gap. Panel (a) shows the fictitious free energy landscape, and (b) the corresponding free energy derivative, which equals the chemical potential difference $\Delta\mu$.

To overcome this limitation, the so-called variance-constrained semigrand canonical ensemble (VC-SGC) has been proposed [14]. In this ensemble, the term $N_{\text{tot}}c\Delta\mu$ is replaced for a term that does not only drive the concentration, but also constrains its fluctuations. Specifically, the density function can be expressed as [13]

$$\rho = \exp \left[-\beta(E + \bar{\kappa}N(c + \bar{\phi}/2)^2) \right]. \quad (3.37)$$

The VC-SGC ensemble thus introduces the two fixed quantities $\bar{\phi}$ and $\bar{\kappa}$, which drive the concentration and the fluctuation of the concentration, respectively. To see this, note that when $c = -\bar{\phi}/2$, the second term in the exponential is at a minimum (0). If c deviates from this value, the excess energy is amplified by $\bar{\kappa}$; for a large value of $\bar{\kappa}$ the argument of the exponential will be high, and ρ consequently low. Thus the density ρ will be maximum at $c = -\bar{\phi}/2$ and then die off with c as a Gaussian, where a large $\bar{\kappa}$ means more rapidly decreasing ρ . By choosing a sufficiently large value of $\bar{\kappa}$, a choice of $\bar{\phi}$ will hence, in practice, map to one and only one concentration.

The above mentioned ensembles and their related quantities are gathered in Table 3.1. The ensembles can also easily be made isobaric by fixing the pressure and allowing for varying volume.

Table 3.1: *Ensembles used or described in the thesis. SGC and VC-SGC are abbreviations for semigrand canonical and variance-constrained semigrand canonical.*

Ensemble	Constant quantities	Thermodynamic potential	Partition function
Microcanonical	N, V, E	Entropy S	$\Omega = \sum_s 1$
Canonical	N, V, T	Helmholtz F	$\mathcal{Z} = \sum_s e^{-\beta E}$
Grand canonical	μ, V, T	Grand pot. Φ	$\Xi = \sum_s e^{-\beta(E-N\mu)}$
SGC	$\Delta\mu, N_{\text{tot}}, V, T$	SG pot. Ψ	$\Upsilon = \sum_s e^{-\beta(E-N_{\text{tot}}c\Delta\mu)}$
VC-SGC	$\bar{\phi}, \bar{\kappa}, N_{\text{tot}}, V, T$	VC-SGC pot.	$\Theta = \sum_s e^{-\beta(E+\bar{\kappa}N(c+\bar{\phi}/2)^2)}$

3.2 Atomistic modeling

In an experiment we are typically interested in measuring an observable dependent on the microstate, e.g., temperature or pressure. Such a measurement is never instantaneous but rather averaged over a time t . During that time, the microstate will evolve and thereby visit other microstates in the ensemble. If we denote the observable with $f(\mathbf{r}(t), \mathbf{p}(t))$, we may describe the measurement as

$$\bar{f} = \lim_{t \rightarrow \infty} \frac{1}{t} \int_0^t f(\mathbf{r}(t'), \mathbf{p}(t')) dt'. \quad (3.38)$$

We may now ask ourselves whether such a measurement can be predicted by ensemble theory. If we happen to know everything about the ensemble at hand, we can compute the expectation value of the observable in that ensemble,

$$\langle f \rangle = \frac{\int f(\mathbf{r}, \mathbf{p}) \rho(\mathbf{r}, \mathbf{p}) d\mathbf{r} d\mathbf{p}}{\int \rho(\mathbf{r}, \mathbf{p}) d\mathbf{r} d\mathbf{p}} \quad (3.39)$$

and one often assumes that

$$\bar{f} = \langle f \rangle, \quad (3.40)$$

which is referred to as the ergodic hypothesis.

Atomistic simulations will typically compute observables according to either Eq. (3.38) or (3.39). The choice of approach should be determined by how efficiently the respective quantities can be evaluated in the phase space at hand. In this section, Molecular Dynamics and Monte Carlo simulations are introduced. The former is essentially a method to simulate Eq. (3.38), while the latter attempts to efficiently evaluate Eq. (3.39).

3.2.1 Molecular Dynamics simulations

By choosing an initial configuration (\mathbf{r}, \mathbf{p}) and defining an interatomic potential, we can use a computer to solve Newton's equation of motions for large numbers

of particles. If we allow the system to equilibrate and then conduct a long enough simulation, we can evaluate observables in the spirit of Eq. (3.38). Such a simulation, however, is usually not fully satisfactory. Since Newton's equations of motion conserve energy, a straightforward Molecular Dynamics simulation corresponds to constant (N, V, E) , i.e. it will sample the microcanonical ensemble. Usually, we would rather want to have constant (N, V, T) (the canonical ensemble) or even (N, P, T) (the isobaric-isothermal ensemble). This can be accomplished by adding a thermostat and/or barostat to the system. The system is then forced to maintain a certain temperature and pressure, respectively.

It is important to note that a Molecular Dynamics simulation will resemble a real system in the sense that energy barriers will severely prevent the system from attaining all possible configurations. In a system where atoms are more or less confined to a position in a lattice, such as a metal, the atoms will only rarely change places. Therefore, in a system where not all atoms are equal, such as an alloy, a different approach is required.

3.2.2 Monte Carlo integration

The challenge of simulating an alloy can be approached with Monte Carlo simulations. After an initial microstate is chosen, subsequent steps are not determined through time propagation as in Molecular Dynamics simulations, but rather through a random walk in phase space. By doing a sufficiently long random walk, all of phase space is sampled and any computed observable within the Monte Carlo method will therefore represent an ensemble average in the spirit of Eq. (3.39).

The random walk through phase space is guided by the density function ρ . A trial step is chosen at random, but the step may be rejected. The probability of accepting a trial step is given by the ratio of the density function between the trial state and the current state or 1 if the ratio exceeds one,

$$P(\text{accept}) = \min \{1, \rho(\text{trial})/\rho(\text{current})\}. \quad (3.41)$$

This scheme is referred to as the Metropolis algorithm [15]. The integral in Eq. (3.39) is then by no means evaluated from a uniform sampling over phase space but rather through so-called importance sampling, where the most important parts of phase space are visited more often.

3.2.3 Atomistic modeling of alloys

Alloys can be studied efficiently by combining Molecular Dynamics and Monte Carlo simulations. To this end, a Molecular Dynamics simulation is interrupted every few timesteps for Monte Carlo trial steps, where the identities of randomly selected atoms are swapped. The swapping can be done in different ways, corresponding to sampling of different ensembles.

The perhaps most straightforward method is to randomly select two non-identical atoms, and swap their identities, i.e. in the case of Pd-Au, the Pd becomes Au and vice versa. The number of each species is thus conserved. The change in

energy ΔE is calculated, and the acceptance probability is computed from the ratio of Boltzmann factors,

$$P = \min \{1, \exp [-\beta \Delta E]\}. \quad (3.42)$$

This method samples the canonical ensemble and it is often used for Monte Carlo simulations of binary alloys. From a computational perspective, however, the canonical ensemble suffers from the disadvantage of being impractical for parallel computing [14].

A different approach is to only choose one atom randomly and change its identity. The concentration does then change and by fixing a chemical potential difference $\Delta\mu$, we can compute a probability of acceptance from the semigrand canonical ensemble density functions,

$$P = \min \{1, \exp [-\beta (\Delta E + N_{\text{tot}} \Delta c \Delta \mu)]\} \quad (3.43)$$

where Δc is the change in concentration introduced by the trial. $\Delta\mu$ thus provides a driving force, driving the system to a certain concentration. This method is suitable for parallelization, but suffers from a major problem. As stated already in Section 3.1.4, it does not allow for sampling inside a miscibility gap – the simulations would always end up at a concentration on either side of the gap. This shortcoming can be overcome with the VC-SGC ensemble and Eq. (3.43) becomes

$$P = \min \left\{ 1, \exp \left[-\beta \left(\Delta E + \bar{\kappa} N_{\text{tot}} \Delta c \left(\bar{\phi} + \Delta c + 2c \right) \right) \right] \right\} \quad (3.44)$$

given that we specify $\bar{\phi}$ and $\bar{\kappa}$. With a sufficiently high value of $\bar{\kappa}$, the system will also stabilize concentrations inside the miscibility gap.

3.3 Electronic structure modeling

While the atomic configurations in alloyed nanoparticles can be described well with classical statistical mechanics, the accuracy of the results will be bounded by the quality of the interatomic potential that is used. Further, atomistic modeling can not make predictions of the optical response of a nanoparticle. In order to truly understand the plasmonics of metal nanoparticles, we therefore need to turn to first-principles methods. This section describes the widespread and well established electronic structure modeling method density functional theory, used to efficiently calculate the ground state in a system of many electrons. For the optical response, the ground state calculation will not be sufficient, and time-dependent density functional theory is introduced. The section is strongly inspired by Ref. 16.

3.3.1 Density functional theory

Consider a system with N interacting electrons. Density functional theory (DFT) deals with the problem of solving the Schrödinger equation

$$\hat{H}_0 \psi_j(\mathbf{r}_1, \dots, \mathbf{r}_N) = E_j \psi_j(\mathbf{r}_1, \dots, \mathbf{r}_N), \quad (3.45)$$

where \hat{H}_0 is the Hamiltonian of the system, ψ_j are the wave functions with corresponding energy E_j , and \mathbf{r}_i represents the spatial coordinates of the i -th particle. A reasonable expression for the Hamiltonian would be

$$\hat{H}_0 = - \sum_{i=1}^N \frac{1}{2} \nabla_i^2 + \sum_{i=1}^N v(\mathbf{r}_i) + \sum_{i,j=1, i \neq j}^N w(|\mathbf{r}_i - \mathbf{r}_j|). \quad (3.46)$$

The first term represents the kinetic energy of the electrons, the second term represents the potential energy from the ions and the third term represents the interaction between the electrons. The next step would then be to solve the Schrödinger equation (3.45), obtaining the wavefunctions ψ_j and the corresponding energies. The wavefunction, however, is dependent on $3N$ spatial coordinates, and the combinatorics of such a system quickly blows up. It is therefore impractical to solve the Schrödinger equation for more than two particles. DFT, however, provides an alternative approach in which we, instead of the wavefunctions, can work with the three-dimensional electron density

$$n(\mathbf{r}) = N \int d^3\mathbf{r}_2 \dots \int d^3\mathbf{r}_N |\psi(\mathbf{r}, \mathbf{r}_2, \dots, \mathbf{r}_N)|^2. \quad (3.47)$$

The direct approach to calculating $n(\mathbf{r})$ would be to get the electron density from the Hamiltonian by solving the Schrödinger equation,

$$v(\mathbf{r}) \rightarrow \hat{H}_0 \rightarrow \{\psi_j\} \rightarrow n(\mathbf{r}). \quad (3.48)$$

The first Hohenberg-Kohn theorem [17] states that there is a one-to-one relationship between the ground state electron density $n_0(\mathbf{r})$ and the potential $v(\mathbf{r})$. This establishes the wave functions as a functional of the ground state density, because if we know the density, we may in principle reconstruct the potential, which gives the Hamiltonian, which leads to the wave functions:

$$n_0(\mathbf{r}) \rightarrow v(\mathbf{r}) \rightarrow \hat{H}_0 \rightarrow \{\psi_j\}. \quad (3.49)$$

This means that any observable can be expressed as a functional of the ground state density,

$$O[n_0] = \langle \psi[n_0] | \hat{O} | \psi[n_0] \rangle. \quad (3.50)$$

In particular, this means that the density minimizing the functional

$$E[n] = \langle \psi[n] | \hat{H}_0 | \psi[n] \rangle \quad (3.51)$$

really is the ground state density, thanks to the variational principle. This is referred to as the second Hohenberg-Kohn theorem [17].

The Hohenberg-Kohn theorems are of practical importance only if we can calculate the density without taking the detour in Eq. (3.48). A framework for doing so was provided by Kohn and Sham [18]. In their formalism, we work with noninteracting electrons and the ground state density is then written as a sum

$$n_0(\mathbf{r}) = \sum_{i=1}^N |\phi_i(\mathbf{r})|^2 \quad (3.52)$$

where ϕ_i are solutions to the Kohn-Sham equation,

$$\left(-\frac{1}{2}\nabla^2 + v'[n](\mathbf{r})\right)\phi_i(\mathbf{r}) = \epsilon_i\phi_i(\mathbf{r}). \quad (3.53)$$

Equation (3.53) has the huge advantage that it is an equation in only 3 spatial coordinates, as opposed to the original problem having $3N$ coordinates.

It should be noted that in order for Eq. (3.52) to actually be the ground state density, the potential v' in Eq. (3.53) cannot be the same as v in Eq. (3.46). Instead v' is *defined* in such a way that the ground state is recovered through Eq. (3.52). The problem then comes down to choosing v' in a clever way. It is usually expressed as a sum of three different parts,

$$v'[n](\mathbf{r}) = v_0(\mathbf{r}) + v_{\text{H}}[n](\mathbf{r}) + v_{\text{xc}}[n](\mathbf{r}). \quad (3.54)$$

Here $v_0(\mathbf{r})$ is identical to $v(\mathbf{r})$ in Eq. (3.46), i.e. the potential from the ions. The Coulomb interaction is partly accounted for by $v_{\text{H}}(\mathbf{r})$, the Hartree potential, given by

$$v_{\text{H}}[n](\mathbf{r}) = \int d^3\mathbf{r}' \frac{n(\mathbf{r}')}{|\mathbf{r} - \mathbf{r}'|}. \quad (3.55)$$

What is left is gathered into $v_{\text{xc}}[n](\mathbf{r})$, the so-called exchange-correlation functional. The result of a DFT calculation will be no better than the choice of this functional, whence a lot of effort has been put into developing accurate exchange-correlation functionals.

3.3.2 Time-dependent density functional theory

If we want to study dynamic phenomena – such as LSPR – the Schrödinger equation (3.45) and DFT alone are insufficient. Instead we need to turn to time-dependent density functional theory (TDDFT) and the time-dependent Schrödinger equation,

$$\hat{H}(t)\Psi_j(\mathbf{r}_1, \dots, \mathbf{r}_N, t) = i\frac{\partial}{\partial t}\Psi_j(\mathbf{r}_1, \dots, \mathbf{r}_N, t). \quad (3.56)$$

This is no longer an eigenvalue, but an initial value problem. The solution will thus be dependent on the initial wavefunction, denoted Ψ_0 . The Hamiltonian $\hat{H}(t)$ can be expressed in the same way as in Eq. (3.46), except that we need to allow for the potential v to be dependent on time.

Runge and Gross [19] proved that there exists a one-to-one relationship between electron density and potential, just as in the time-independent case. Now, however, a few more conditions have to be fulfilled. Two potentials are considered different only if they differ by a constant dependent on space (i.e. $v(\mathbf{r}, t) + c(\mathbf{r})$ is *not* considered different from $v(\mathbf{r}, t)$, but $v(\mathbf{r}, t) + c(t)$ is). It must also be possible to expand $v(\mathbf{r}, t)$ in a Taylor series around the initial time. Then, for a given initial state Ψ_0 , a given density $n(\mathbf{r}, t)$ cannot be the result of two different potentials, and a given $v(\mathbf{r}, t)$ can only result in one $n(\mathbf{r}, t)$. This provides theoretical support for writing

$$n_0(\mathbf{r}, t) \rightarrow v(\mathbf{r}, t) \rightarrow \hat{H}_0(\mathbf{r}, t) \rightarrow \{\psi_i(\mathbf{r}, t)\} \quad (\text{fixed } \Psi_0). \quad (3.57)$$

In a fashion analogous to the time-independent case, we can now write any observable as a functional of the electron density and the initial state,

$$O[n, \Psi_0](t) = \langle \Psi[n, \Psi_0](t) | \hat{O} | \Psi[n, \Psi_0](t) \rangle. \quad (3.58)$$

Just as in the time-independent case, we still need a way to calculate $n_0(\mathbf{r}, t)$. The time-dependent version of the Kohn-Sham equation reads

$$\left(-\frac{1}{2} \nabla^2 + v'[n](\mathbf{r}, t) \right) \phi_i(\mathbf{r}, t) = i \frac{\partial}{\partial t} \phi_i(\mathbf{r}, t) \quad (3.59)$$

and just as before, v' is defined so that the density is recovered from the Kohn-Sham orbitals through

$$n(\mathbf{r}, t) = \sum_{i=1}^N |\phi_i(\mathbf{r}, t)|^2. \quad (3.60)$$

The potential v' is now not only dependent on the density n but also the initial state Ψ_0 and the initial Kohn-Sham state Φ_0 . It is usually divided into three parts just as in the time-independent case,

$$v'[n, \Psi_0, \Phi_0](\mathbf{r}, t) = v_0(\mathbf{r}, t) + v_H[n](\mathbf{r}, t) + v_{xc}[n, \Psi_0, \Phi_0](\mathbf{r}, t), \quad (3.61)$$

where v_0 is the potential from the ions, v_H is the Hartree potential as in Eq. (3.55) (but with a time-dependent density n), and v_{xc} is the exchange-correlation functional. A good choice of v_{xc} is crucial to get accurate results from a TDDFT calculation. Compared to the time-independent case, v_{xc} could now be a functional of all previous densities, but very often an adiabatic v_{xc} is chosen, in which case only the instantaneous density enters the functional. In that case, the same functionals as in the time-independent case can be used.

3.3.3 The projector augmented wave method

Even though the Kohn-Sham equation (3.59) has the form of a one-electron Schrödinger equation and thus is a great simplification of the full many-body problem, it is still far from trivial to solve. From a numerical perspective, the main problem is that the wave functions oscillate rapidly close to the ion cores, while they are much smoother in the interstitial regions. The different behaviors call for different numerical representations, but luckily there are several methods to overcome this problem. In this thesis, a DFT code based on the projector augmented wave (PAW) formalism [20] has been used. Briefly, one works with pseudo wave functions $\tilde{\phi}$ that are related to the Kohn-Sham wave functions by

$$\phi(\mathbf{r}, t) = \hat{T} \tilde{\phi}(\mathbf{r}, t) \quad (3.62)$$

where the transformation \hat{T} is defined in such a way that $\tilde{\phi}$ is much smoother. The time-dependent Kohn-Sham equation (3.59) can then be rewritten,

$$\left[\left(-i \frac{\partial}{\partial t} \right) \hat{T} + \hat{H}_{KS}(t) \hat{T} \right] \tilde{\phi}_i(\mathbf{r}, t) = 0. \quad (3.63)$$

The pseudo-wavefunctions can further be expressed as linear combinations of atomic orbitals $\tilde{\varphi}_\mu$ centered at the atoms,

$$\tilde{\phi}_i(\mathbf{r}, t) = \sum_{\mu} C_{\mu i}(t) \tilde{\varphi}_\mu(\mathbf{r} - \mathbf{R}^\mu) \quad (3.64)$$

where the sum runs over all orbitals, centered at each atom.

To propagate the system in time, Eq. (3.64) is inserted into the Kohn-Sham equation (3.63), and it is multiplied with \hat{T}^\dagger from the left,

$$\left[\hat{T}^\dagger \left(-i \frac{\partial}{\partial t} \right) \hat{T} + \hat{T}^\dagger \hat{H}_{KS}(t) \hat{T} \right] \sum_{\mu} C_{\mu i}(t) \tilde{\varphi}_\mu(\mathbf{r} - \mathbf{R}^\mu) = 0. \quad (3.65)$$

One can then multiply with $\tilde{\varphi}_\nu^*$ and integrate,

$$\sum_{\mu} \left[\left(-i \frac{\partial C_{\mu i}(t)}{\partial t} \right) \langle \tilde{\varphi}_\nu | \hat{T}^\dagger \hat{T} | \tilde{\varphi}_\mu \rangle + C_{\mu i}(t) \langle \tilde{\varphi}_\nu | \hat{T}^\dagger \hat{H}_{KS}(t) \hat{T} | \tilde{\varphi}_\mu \rangle \right] = 0. \quad (3.66)$$

By writing $S_{\nu\mu} = \langle \tilde{\varphi}_\nu | \hat{T}^\dagger \hat{T} | \tilde{\varphi}_\mu \rangle$ and $H_{\nu\mu} = \langle \tilde{\varphi}_\nu | \hat{T}^\dagger \hat{H}_{KS}(t) \hat{T} | \tilde{\varphi}_\mu \rangle$, Eq. (3.66) can be expressed in matrix form,

$$i\mathbf{S} \frac{d\mathbf{C}(t)}{dt} = \mathbf{H}(t)\mathbf{C}(t), \quad (3.67)$$

where \mathbf{S} is independent of time, \mathbf{H} changes in each time step and \mathbf{C} is the unknown coefficient matrix.

3.3.4 Time-propagation and optical absorption

Equation (3.67) can be solved with a semi-implicit Crank-Nicolson method. We step forward with a timestep Δt , and in each step we use the discretization

$$\frac{d\mathbf{C}(t)}{dt} \approx \frac{\mathbf{C}(t + \Delta t) - \mathbf{C}(t)}{\Delta t}. \quad (3.68)$$

The discretized version of Eq. (3.67) is then

$$i\mathbf{S} \frac{\mathbf{C}(t + \Delta t) - \mathbf{C}(t)}{\Delta t} = \mathbf{H}(t) \frac{1}{2} (\mathbf{C}(t) + \mathbf{C}(t + \Delta t)) \quad (3.69)$$

or rewritten

$$\left[\mathbf{S} + i \frac{\Delta t}{2} \mathbf{H}(t) \right] \mathbf{C}(t + \Delta t) = \left[\mathbf{S} - i \frac{\Delta t}{2} \mathbf{H}(t) \right] \mathbf{C}(t), \quad (3.70)$$

which can be solved for $\mathbf{C}(t + \Delta t)$ with standard linear algebra routines. The drawback with the form (3.70) is that we had to use $\mathbf{H}(t)$. We would be better off using \mathbf{H} at an intermediate timestep. That is possible when Eq. (3.70) is solved, because we may then calculate $H(t + \Delta t)$ and do the approximation

$$\mathbf{H}(t + \Delta t/2) = \frac{\mathbf{H}(t) + \mathbf{H}(t + \Delta t)}{2}. \quad (3.71)$$

We can then solve the system

$$\left[\mathbf{S} + i \frac{\Delta t}{2} \mathbf{H}(t + \Delta t/2) \right] \mathbf{C}(t + \Delta t) = \left[\mathbf{S} - i \frac{\Delta t}{2} \mathbf{H}(t + \Delta t/2) \right] \mathbf{C}(t) \quad (3.72)$$

yielding a presumably more accurate $\mathbf{C}(t + \Delta t)$ [21].

With this method, the optical absorption can be found by applying a delta pulse of electromagnetic field as an external potential at $t = 0$, and propagate in time, recording the time evolution of the dipole moment

$$\mathbf{p}(t) = \int \mathbf{r} n(\mathbf{r}, t) d^3r. \quad (3.73)$$

As seen in Chapter 2, the Fourier transform of the dipole moment is related to the electric field via

$$\hat{\mathbf{p}}(\omega) \propto \alpha(\omega) \hat{\mathbf{E}} \quad (3.74)$$

and since the Fourier transform $\hat{\mathbf{E}}$ of a delta pulse is just a constant, we have $\hat{p}_x(\omega) \propto \alpha(\omega)$, where p_x is the dipole moment in the direction of the kick. The cross section of absorption can then be evaluated as

$$C_{\text{abs}} \propto \omega \text{Im} [\alpha(\omega)] = \omega \text{Im} [\hat{p}_x(\omega)] \quad (3.75)$$

in accordance with Eq. (2.14).

4

Thermodynamics of Pd-Au alloys

While the study of homogeneous metals is challenging, the situation is even more complex in an alloy. In addition to the zoo of questions that surrounds any material, a study of alloys should take into account the different ways the elements in the material may be ordered.

This chapter presents the results from atomistic modeling of Pd-Au alloys and is essentially split into three parts. In the first part, the thermodynamic behavior of bulk Pd-Au is studied. In nanoparticles, a large proportion of the atoms are located on surface sites and surface properties of the material are therefore highly important. Accordingly, the second part deals with flat surfaces. In the third part, nanoparticles with different sizes and shapes are introduced, with the results from the bulk and surface part as guidance.

4.1 Computational details

All calculations were performed in the Molecular Dynamics (MD) code LAMMPS [22] using the Pd-Au EAM potential published by Marchal et al. [23]. The simulations were performed as a hybrid of MD and Monte Carlo (MC) simulations, as described in Chapter 3. MD simulations were run using a Nòse-Hoover thermostat, leading to constant temperature, and in the case of bulk samples also with a Nòse-Hoover barostat imposing zero pressure. The thermo and barostats were used with damping parameters of 600 and 20 600 timesteps, respectively, and the length of one timestep was set to 2.5 fs.

With the exception of Section 4.5, the simulations were run in the semigrand canonical ensemble. Pd-Au has no miscibility gap [24] and by specifying the chemical potential difference $\Delta\mu$, we may therefore expect to end up at one and only one concentration. The simulations were performed for values of $\Delta\mu$ ranging from -1.5 to 0.5 eV/atom. $\Delta\mu$ was swept in sequence, so that the last configuration for one value of $\Delta\mu$ was used as input to the simulations at the next value of $\Delta\mu$. With this method equilibration is speeded up significantly, and only the first 1000 MD steps had to be discarded for each value of $\Delta\mu$. In total, the simulations ran at least 10^4 MD steps for each value of $\Delta\mu$. Every 100th MD step, $0.4N$ trial MC swaps were carried out, where N is the number of atoms in the simulation.

4.2 Bulk properties

Bulk simulations were performed with a cell comprising 2048 atoms and periodic boundary conditions. Table 4.1 summarizes two properties related to bulk Pd and Au, lattice parameter and cohesive energy. Note that the lattice parameter is slightly overestimated. The cohesive energy in Pd agrees well with experiment, while the Au cohesive energy is overestimated. These deviations are consequences of the PBE functional used for the DFT calculations to which the potential was fit, as pointed out in Ref. 23.

Table 4.1: *Bulk properties at 0 K as obtained with the EAM potential [23], with comparison to experimental values taken from Ref. 25.*

Quantity	Pd		Au	
	EAM	Expt.	EAM	Expt.
Lattice parameter (Å)	3.97	3.89	4.19	4.08
Cohesive energy (eV)	-3.70	-3.89	-2.99	-3.81

It is now interesting to see how the potential energy varies as a function of concentration. Specifically, we are interested in the mixing energy

$$U_{\text{mix}} = U(c) - cU(1) - (1 - c)U(0), \quad (4.1)$$

which is a measure of the potential energy gained by alloying the two elements. Figure 4.1(a) shows U_{mix} per atom for different temperatures as obtained with MD/MC. U_{mix} is negative for all values of c , which indicates that the system is miscible in all proportions. Figure 4.1(a) also contains energies reported in Ref. 23, obtained with DFT calculations using the PBE functional. These correspond to the mixing energy at 0 K. PBE apparently predicts a smaller mixing energy than the EAM potential, which may have some impact on the segregation.

The configuration of atoms in an alloy at finite temperature is determined by the free energy, defined by

$$F = U - TS. \quad (4.2)$$

Equation (4.2) can be viewed as a representation of the competition between energy and entropy. Mixing two species of atoms increases the entropy of the system and may thus lead to lower free energy even if the mixing energy is positive. A highly ordered structure, on the other hand, may be favorable if it leads to substantially lower potential energy.

The free energy is not directly observable in a MD/MC simulations. The chemical potential difference $\Delta\mu$ and the concentration c are readily available though. We may thus use the relationship

$$\Delta\mu = -\frac{1}{N_{\text{tot}}} \frac{\partial F}{\partial c} \quad (4.3)$$

as derived in Chapter 3, and obtain the free energy by integration (here $c = N_{\text{Pd}}/N_{\text{tot}}$ and $\Delta\mu = \mu_{\text{Au}} - \mu_{\text{Pd}}$). Thus we integrate $\Delta\mu$ to obtain the Helmholtz free energy

per particle as

$$\Delta F(c) = - \int_0^c \Delta \mu \, dc'. \quad (4.4)$$

We may do the same construction as in Eq. (4.1) to study the mixing free energy,

$$F_{\text{mix}} = F(c) - cF(1) - (1-c)F(0). \quad (4.5)$$

The result is shown in Fig. 4.1(c). The difference between the mixing energy and the mixing free energy is essentially that entropy is added to the latter, so that the energy wells are deeper and smoother.

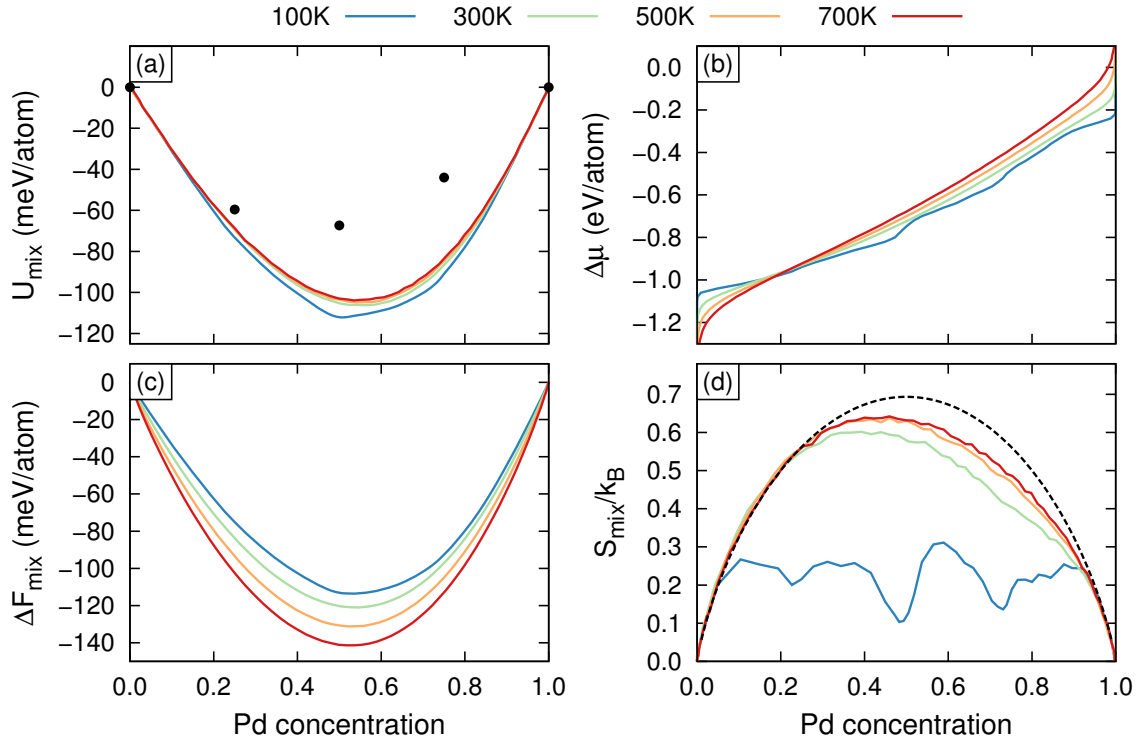


Figure 4.1: Thermodynamics of bulk Pd-Au obtained with MD/MC simulations. (a) Mixing potential energy U_{mix} . The black points represent DFT results obtained with the PBE functional presented in Ref. 23. (b) Chemical potential difference $\Delta\mu$, (c) mixing free energy ΔF_{mix} , and (d) entropy of mixing S_{mix} . The dashed black line shows entropy of ideal mixing, i.e. Eq. (4.8).

The entropy can be calculated by rearranging Eq. (4.2):

$$S = \frac{U - F}{T} \quad (4.6)$$

and the entropy of mixing may be defined in the same manner,

$$S_{\text{mix}} = \frac{U_{\text{mix}} - F_{\text{mix}}}{T}. \quad (4.7)$$

The entropy thus calculated is shown in Fig. 4.1(d). It is important to note that the entropy captured in an MD/MC simulation is not only that due to the different

configurations of Pd and Au but also due to vibrations in the lattice. By defining the mixing entropy in Eq. (4.7), much of the vibrational entropy is canceled, given the assumption that the vibrational entropy of the mixed system is close to a weighted average of the vibrational entropies of the pure systems. Thus, S_{mix} should primarily contain the configurational entropy.

In Fig. 4.1(d), the calculated entropy of mixing is also compared to the (configurational) entropy of ideal mixing,

$$S_{\text{ideal mix}} = -k_{\text{B}} (c \ln c + (1 - c) \ln(1 - c)), \quad (4.8)$$

shown with the dashed black line. All calculated curves are below the entropy of ideal mixing, which is expected; the dashed black line is to be understood as the maximum possible entropy. As the temperature is raised, the entropies approach the entropy of ideal mixing. This is also expected since entropy should dominate over potential energy at high temperatures. Entropies well below the entropy of ideal mixing can be explained with potential energy; ordering the atoms lowers the potential energy enough to lower the free energy in spite of the entropic penalty $-TS$. The low-entropy regions therefore correspond to concentrations where the system finds an ordered structure.

4.2.1 Searching for ordered configurations

One of the goals of this thesis is to find out to what extent ordering of the atoms in an alloyed nanoparticle affects the plasmonic properties. To this end, we need to compare ordered nanoparticles to nanoparticles with randomly distributed atoms. In this context, structures with low entropy are particularly interesting. Note that the low entropy regions in Fig. 4.1(d) correspond to regions in $\Delta\mu$ with a high slope. A simple way of searching for ordered structures is thus to search for vertical regions in $\Delta\mu$ vs c plots. This is attractive since those plots are straightforwardly obtained from a Monte Carlo simulation in the semigrand canonical ensemble.

The physical significance of $\Delta\mu$ can be understood in terms of the concept of generalized forces and displacements. Specifically the chemical potential difference $\Delta\mu$ can be regarded as a generalized force driving the concentration, just like a mechanical force would induce a spatial displacement of an object. Physical intuition can be obtained by comparing to a spring with a stiffness varying with displacement.

	“Usual” quantities	“Generalized” quantities
Energy	Pot. energy U	Free energy F
Force	$F = -\frac{dU}{dx}$	$\Delta\mu = -\frac{1}{N} \frac{dF}{dc}$
Displacement	x	c
Stiffness	$\frac{dF}{dx}$	$\frac{d\Delta\mu}{dc}$

An increase in $\Delta\mu$ results in an increase in concentration, just as an increase in force increases the extension of the spring. Nevertheless, when pulling the spring, we are likely to spend more time in the regions with a stiff spring constant. In those

regions, a large interval in the applied force results in roughly the same displacement. In analogy, some intervals of chemical potential difference will result in roughly the same concentration. Those regions are particularly interesting, since they can be viewed as stable concentrations, where the system is in a preferred configuration. Those regions are to be found where $d\Delta\mu/dc$ is high. If choosing a $\Delta\mu$ at random, it is thus slightly more probable to end up with a concentration in those regions.

How does the chemical potential difference relate to conditions in the laboratory? Imagine a solution with free Au and Pd atoms. The chemical potential of the respective species would then generally increase when its concentration in the solution is increased. If a nanoparticle is being grown from solution, intuition tells us that the nanoparticle will primarily contain atoms that are more common in the solution. In a simple picture we may hence say that a difference in concentration in the reservoir leads to a difference in chemical potential, which in turn leads to a certain concentration in the nanoparticle.

4.2.2 Acceptance probability and temperature

The low potential energy in ordered configurations may give rise to computational issues. Recall that the probability of accepting a trial swap is proportional to $\exp[-\beta(\Delta E)]$. If the simulation has obtained a low-energy ordered configuration, most trial swap energies ΔE will be quite high, giving a low probability of accepting a trial swap. Low acceptance probability does, however, mean inefficient sampling, and the results are thus less reliable. A Monte Carlo simulation must therefore not be run at a too low temperature. Figure 4.2 shows the acceptance probability in the MD/MC runs presented in Fig. 4.1. Note the similarities in overall shape of the curves for acceptance probability and entropy.

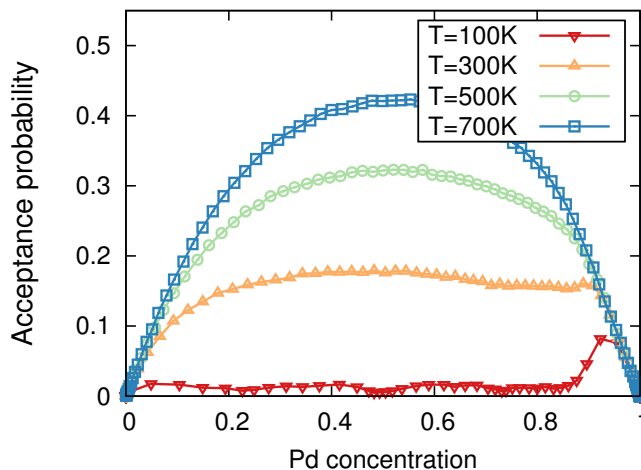


Figure 4.2: Acceptance probability in MD/MC simulations of bulk Pd-Au at different temperatures.

4.3 Surface properties

By creating a slab of material, with surfaces on either side, and periodic boundary conditions in the lateral directions, surface properties of Pd-Au may be investigated.

Crystalline materials are anisotropic, at least on the atomic scale, and slicing up the material therefore leads to different kinds of surfaces depending on the orientation of the cut. Figure 4.3 shows three typical surfaces of a face-centered cubic (fcc) crystal, $\{100\}$, $\{111\}$ and $\{110\}$, which are the ones studied in this thesis. This section aims at comparing these surfaces and describing what happens in a Pd-Au alloy when these surfaces are present. The surface systems were comprised of 25 atomic layers, with a total of 2450, 3000 and 1750 atoms for $\{100\}$, $\{111\}$ and $\{110\}$, respectively.

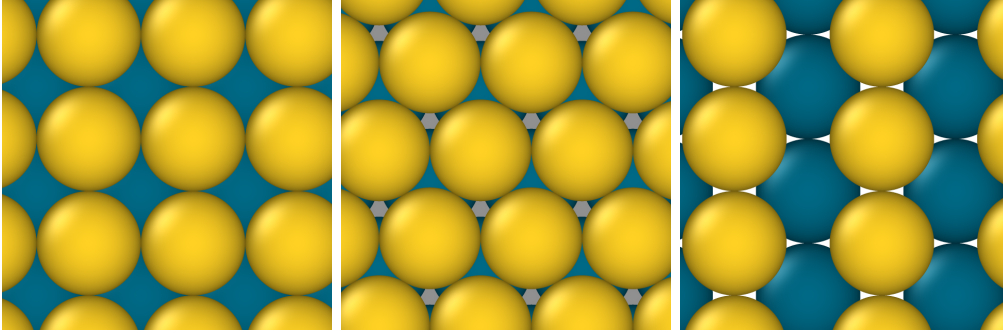


Figure 4.3: Structure of the fcc surfaces investigated in this thesis, left $\{100\}$, middle $\{111\}$ and right $\{110\}$. Yellow atoms represent the surface layer, blue ones subsurface layers, and the gray atoms beneath the $\{111\}$ surface represent the third layer. For the $\{100\}$ and $\{110\}$ surfaces, the atoms of the third layer are situated exactly underneath the surface atoms.

4.3.1 Surface energies

The potential energies of the slab systems were compared to that of the bulk system, to obtain the surface energy via the formula

$$E_{\text{surface}} = N_{\text{slab}} \frac{E_{\text{slab}}/N_{\text{slab}} - E_{\text{bulk}}/N_{\text{bulk}}}{A}, \quad (4.9)$$

where A is the area of the slab exposed to vacuum. Table 4.2 shows the surface energies for $\{111\}$, $\{100\}$ and $\{110\}$ surfaces in Pd and Au. The trend is clear; the $\{111\}$ is energetically favorable, followed by $\{100\}$. The trend agrees with experiment, but the absolute values are substantially lower. This is not entirely surprising, since the EAM potential was fitted to DFT calculations based on the PBE exchange-correlation functional [26], which is known to underestimate surface energies severely.

Table 4.2: Surface energies for Au and Pd of different surfaces, obtained with the EAM potential from Ref. 23, and compared to experimental values taken from Ref. 27.

	Energy (J/m ²)	
	Pd	Au
$\{111\}$	1.37	0.76
$\{100\}$	1.48	0.82
$\{110\}$	1.60	0.92
Exp	2.00	1.50

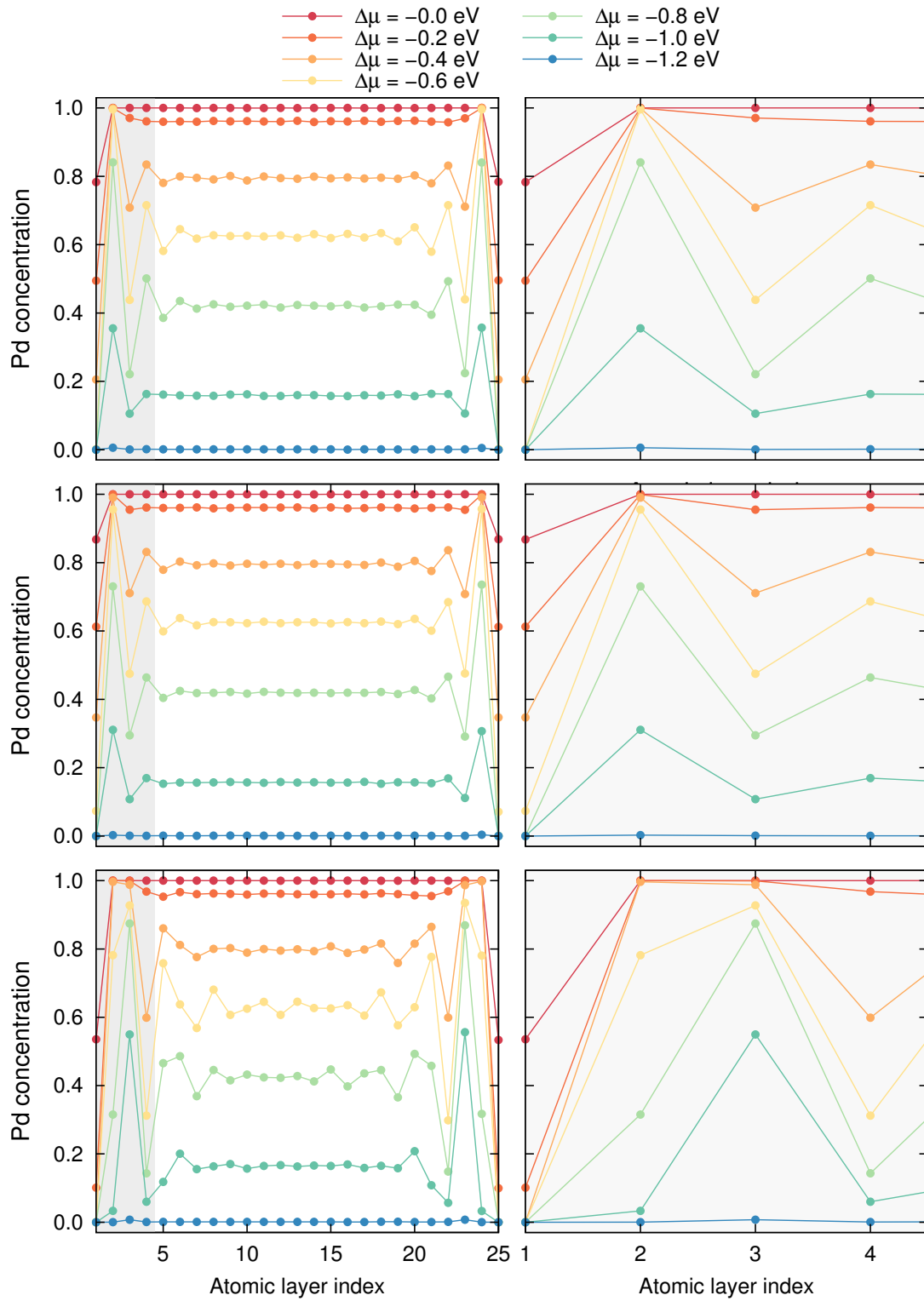


Figure 4.4: Concentration of Pd per atomic layer, for different values of $\Delta\mu$, in a 25 layers thick slab of Pd-Au with $\{100\}$ surfaces (upper), $\{111\}$ surfaces (middle) and $\{110\}$ surfaces (lower) at 300 K. Layer index 1 and 25 correspond to the surface layers. The shaded area in the figures to the left is magnified to the right.

4.3.2 Surface segregation and atomic ordering

Since Pd and Au are miscible, a bulk sample in equilibrium will exhibit a homogeneous distribution of the two elements. Close to a surface, however, the situation may be different. Figure 4.4 shows the concentration profile of the slab systems with the three different surfaces at 300 K. The concentration of palladium in the surface layer is always lower than in the layers beneath. In other words, Au segregates to the surface. In the layer underneath the surface layer, on the other hand, there is excess of Pd. The profiles then exhibit an oscillatory behavior for the outermost five or so layers, before the concentration profile flattens out in the bulk at a concentration determined by $\Delta\mu$. The oscillatory behavior penetrates somewhat deeper in the $\{110\}$ slab, but in that system the atomic layers are closer together; with a unit cell length a the distance between the planes are approximately $0.5a$, $0.58a$ and $0.35a$ for $\{100\}$, $\{111\}$ and $\{110\}$, respectively. If we thus measure in Ångström rather than number of atomic layers, the penetration depth is similar in all three cases.

The surface segregation can be analyzed further by studying the surface concentration as a function of concentration in the bulk as shown in Fig. 4.5. Clearly, the surface concentration of Pd is lower than the bulk concentration, as already noticed in Fig. 4.4. An interesting feature of Fig. 4.5 is the kinks that are present for low temperatures, especially at 100 K, and to some extent also at 300 K. For the $\{100\}$ surface, the kink appears at a surface concentration of 50 %, while for $\{111\}$, there is one kink at approximately 33 % and one at 67 %. This behavior can be understood from visual inspection of the surface geometry. Figure 4.6 shows snapshots from MD/MC simulations at the aforementioned concentrations. Clearly, the kinks correspond to ordered patterns.

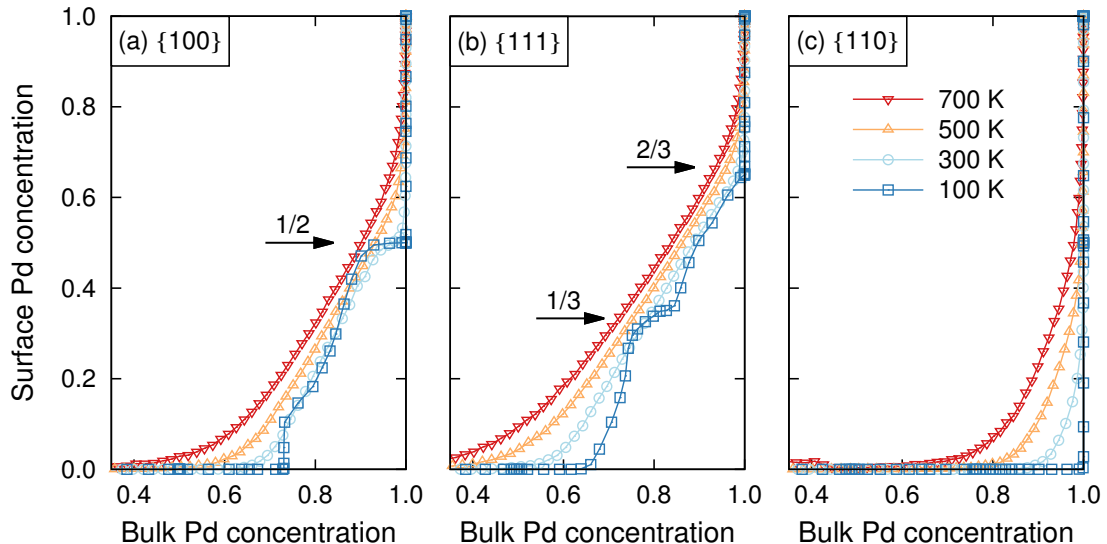


Figure 4.5: Surface concentration of Pd as a function of concentration in the interior of the slab, for $\{100\}$, $\{111\}$ and $\{110\}$ surfaces. The bulk concentrations correspond to the innermost 13 atomic layers. Kinks in the low temperature curves are marked with arrows.

In conclusion, the surface calculations suggest that (i) Au will segregate to

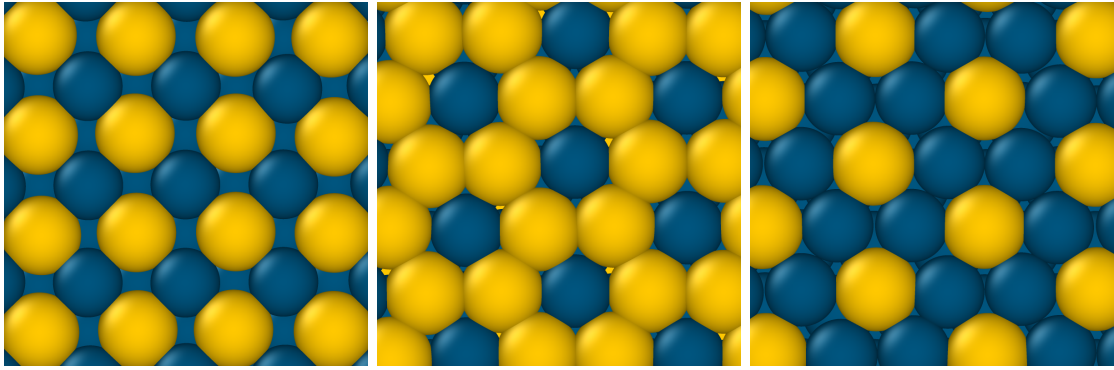


Figure 4.6: Ordered surface configurations corresponding to the kinks in Fig. 4.5, 50 % Pd at $\{100\}$ (left), 33 % at $\{111\}$ (middle) and 67 % at $\{111\}$ (left).

the surface and (ii) there will be ordered patterns on the surface, at least for low temperatures.

4.4 Nanoparticle shapes

Molecular Dynamics simulations usually do not sample all possible shapes a nanoparticle may obtain. Rather, given a reasonable temperature, the shape specified by the initial configuration of the atoms will typically remain similar during the whole simulation. Finding the global energy minimum is therefore a difficult task requiring more sophisticated methods and this section has no intention of being exhaustive in this regard. Generally, however, nanoparticles are non-equilibrium systems; if kinetically permitted they do coarsen. The shape of a nanoparticle is thus not only determined by equilibrium thermodynamics but also by the kinetics of the process by which they are manufactured. Local minima found in an MD/MC simulation therefore deserve closer analysis.

In this section, some highly symmetric shapes are introduced by simple physical reasoning and analytical expressions. Specifically, the discussion will focus on truncated octahedra, constructed from a perfect fcc lattice, and icosahedra, where the lattice is slightly distorted.

4.4.1 The truncated octahedron

Pd and Au both adopt an fcc lattice in the ground state. As shown in Section 4.3.1, $\{111\}$ surfaces are energetically favorable for fcc. The octahedron shown in Fig. 4.7(a) is based on a bulk fcc crystal and terminated by $\{111\}$ surfaces only. Because of the pointy corners, the octahedron still has a fairly high energy. By cutting away these prominent atoms (Fig. 4.7(b)), the energy per atoms is lowered. By cutting more and more layers (Fig. 4.7(c)-(d)), the structure gets more rounded, but at the same time $\{100\}$ surfaces are created, which are higher in energy than $\{111\}$. By cutting enough layers, the structure becomes a cube with $\{100\}$ surfaces only. Ususally there will be an energy minimum somewhere between the octahedron and the cube, where there is balance between rounded shape and a large proportion of

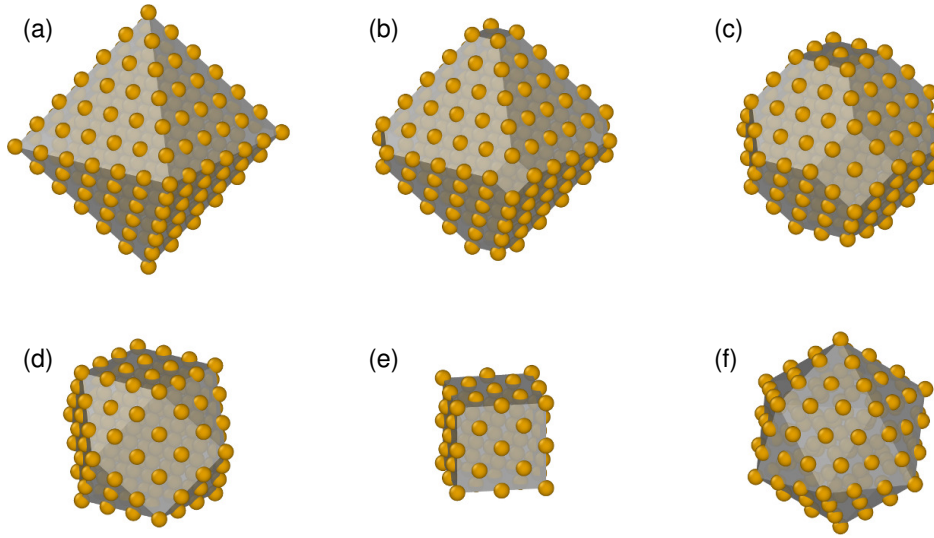


Figure 4.7: *Examples of geometrical structures studied in the thesis. (a) is an octahedron and (b)-(e) are constructed by truncating one, two, three and four planes respectively from each corner of the octahedron. (c) is a regular octahedron, (d) a cuboctahedron and (e) a cube. (f) is an icosahedron which cannot be derived from an octahedron without distorting the crystal structure.*

$\{111\}$ surfaces.

The optimal shape can be derived systematically with the so-called Wulff construction. The surface energy can be expressed as

$$E_{\text{surf}} = \sum_j \gamma_j A_j, \quad (4.10)$$

where the sum runs over all surfaces of the particle, γ_j is the corresponding surface energy and A_j the area of the surface. Keeping the volume of the particle constant, the Gibbs-Wulff theorem states that in the lowest energy shape, the distance from the center of the particle to a particular surface is proportional to the surface energy of that surface. For Au and Pd, in which the $\{100\}$ surface is higher in energy than the $\{111\}$ surface, this means that the distance to the $\{100\}$ surface should be longer, which is the case for the moderately truncated particles in Fig. 4.8(b)-(c). Fig 4.8 shows this optimal shape (ignoring $\{110\}$ surfaces, whose inclusion would otherwise have truncated the edges slightly). The shapes are very similar for Au and Pd, and we note that it is very close to being a “regular truncated octahedron” as shown to the right in Fig. 4.8, i.e. a truncated octahedron where the quadratic and hexagonal side facets are equilateral. Regular truncated octahedra will therefore be used as a reference shape, supposedly close to being ideal. They cannot be constructed with any number of atoms, but rather a set of magic numbers given by

$$N_{\text{RTO}} = 16n^3 + 15n^2 + 6n + 1 \quad \text{for } n = 1, 2, 3\dots \quad (4.11)$$

as may be derived from simple geometrical considerations. The four smallest regular truncated octahedra thus contain 38, 201, 586 and 1289 atoms.

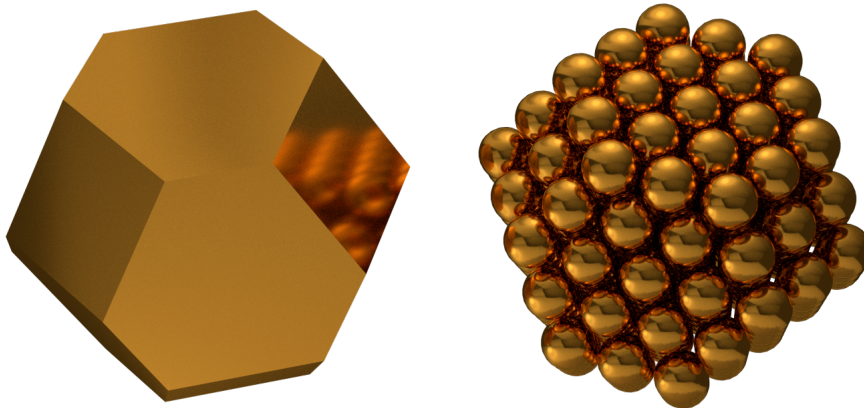


Figure 4.8: *Shape of optimal truncated octahedron (left) and a 201 atom regular truncated octahedron (right).*

Finally, it should be mentioned that the Wulff construction is not intended for really small particles, where edge and corner sites as well as strain make sizeable contributions. The above considerations should therefore only be taken as qualitative. A more elaborate approach will be introduced in Section 4.5.

4.4.2 The icosahedron

A natural question is whether it is possible to construct close-to-spherical particle with $\{111\}$ surfaces only. It turns out that the icosahedron, shown in Fig. 4.7(f) is just that. The icosahedron can be viewed as 20 tetrahedra stacked together with a common vertex. The price paid is some distortion of the fcc structure, leading to strain as well as twin boundaries between the constituent tetrahedra. Icosahedra can be constructed with magic numbers of atoms given by

$$N_{\text{ico}} = \frac{10}{3}n^3 + 5n^2 + \frac{11}{3}n + 1 \quad \text{for } n = 1, 2, 3, \dots \quad (4.12)$$

corresponding to 13, 55, 147 and 561 atoms for the smallest four icosahedra.

For small particles of some metals, it turns out that the icosahedron is lower in energy than any truncated octahedron. As a matter of fact, if one starts an MD simulation at a sufficiently high temperature with a small cuboctahedron of Pd or Au (such as the one in Fig. 4.7(d)), the system spontaneously transforms into an icosahedral shape, lowering its energy. In general, the transformation does not happen by simple relaxation of the structure. Instead a finite temperature needs to be added, reflecting the existence of an energy barrier between the two structures. As a first attempt to compute this barrier, the positions for all atoms in the cuboctahedral and the icosahedral shape was interpolated. To this end, a linear scaling parameter λ is defined, taking the system from the cuboctahedron to the icosahedron through

$$\mathbf{R}_{\text{intermediate}} = \mathbf{R}_{\text{cuboctahedron}} + \lambda (\mathbf{R}_{\text{icosahedron}} - \mathbf{R}_{\text{cuboctahedron}}), \quad (4.13)$$

where \mathbf{R} represents the spatial coordinates for all atoms in the particle. We may then probe the energy landscape by measuring the energy for $0 \leq \lambda \leq 1$. The result is shown in Fig. 4.9. The energies are measured relative to $E(\lambda = 0)$ and normalized by the number of atoms in the particle. Note that the height of the barrier increases with increasing number of atoms, while the energy differences between the two structures decrease. A cuboctahedron should thus be less and less prone to transform into an icosahedron with increasing size. It must be stressed though that the linear interpolation in Eq. (4.13) does not necessarily provide the lowest energy pathway, and the barriers in Fig. 4.9 should thus only be viewed as qualitative.

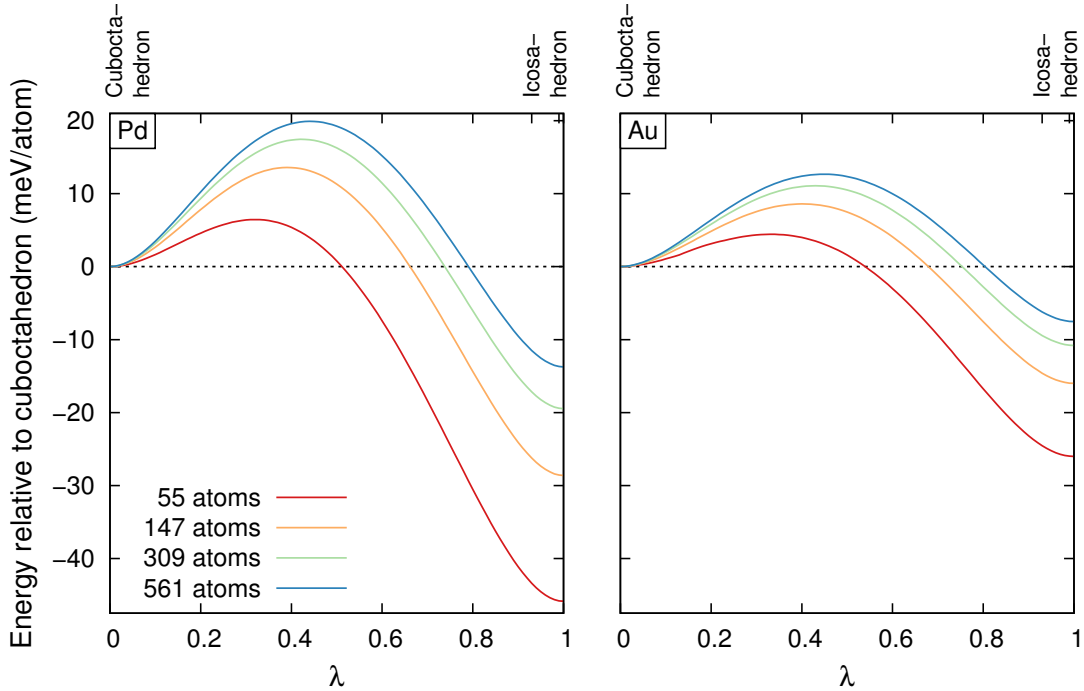


Figure 4.9: Energy landscape along linear interpolation between cuboctahedron and icosahedron. The left and rightmost structures are relaxed cuboctahedra and icosahedra, respectively.

4.4.3 Icosahedra versus regular truncated octahedra

The cuboctahedron is not the truncated octahedron of lowest energy. It is perhaps more interesting to compare icosahedra to regular truncated octahedra, i.e. truncated octahedra with square and regularly hexagonal faces. Such a comparison is not entirely straightforward since particles in these shapes generally contain different number of atoms – we may construct icosahedra with $N = 55, 147, 309, 561, \dots$ atoms, but regular truncated octahedra with $N = 38, 201, 586, \dots$ atoms. To compare these structures, we thus need to make a fit to interpolate between the particle sizes. To this end, we model the energy as

$$E = NE_{\text{coh}} + \sum_j \gamma_j A_j, \quad (4.14)$$

where the first term represents the bulk cohesive energy, and the second term involves the surface energies for different orientations. We note that for a given geometry,

all areas A_j should scale with the diameter squared or equivalently $N^{2/3}$. Thus we may rewrite Eq. (4.14) slightly,

$$\frac{E}{N} = E_{\text{coh}} + \frac{1}{N^{1/3}} \sum_j \gamma_j k_j \quad (4.15)$$

where the sum $\sum_j \gamma_j k_j$ is dependent on geometry, but not size. If we plot the energy per atom as a function of $N^{-1/3}$ we should hence obtain an at least approximately linear dependence. Figure 4.10 shows that this is indeed the case, for Pd and Au as regular truncated octahedra and icosahedra. The slopes, corresponding to the average surface energies, are slightly larger for the octahedra, which is a consequence of their $\{100\}$ surfaces. Note, however, that the icosahedra extrapolated to bulk end up at an energy slightly higher than the bulk cohesive energy. This excess energy is related to the energy penalty of the strain and twin boundaries in icosahedra; for truncated octahedra where the lattice is fcc, the lines extrapolate to the bulk cohesive energy.

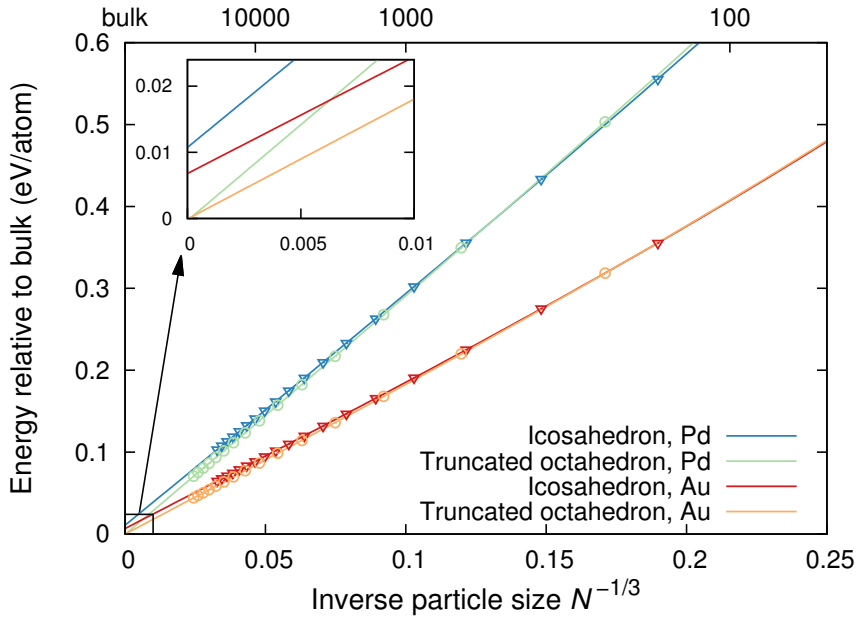


Figure 4.10: Energy per atom relative to bulk energy for Pd and Au regular truncated octahedra and icosahedra, as a function of $N^{-1/3}$. The lines are third degree polynomial fits to the points. The inset shows the behavior in the bulk limit ($N \rightarrow \infty$).

The different behaviors of icosahedra and truncated octahedra result in a crossover between their energies. Figure 4.11 shows the difference between the icosahedra and truncated octahedra lines. The difference changes sign at roughly $N_t = 435$ and 180 for Pd and Au respectively, indicating that icosahedra are lower in energy than regular truncated octahedra for particle sizes below N_t .

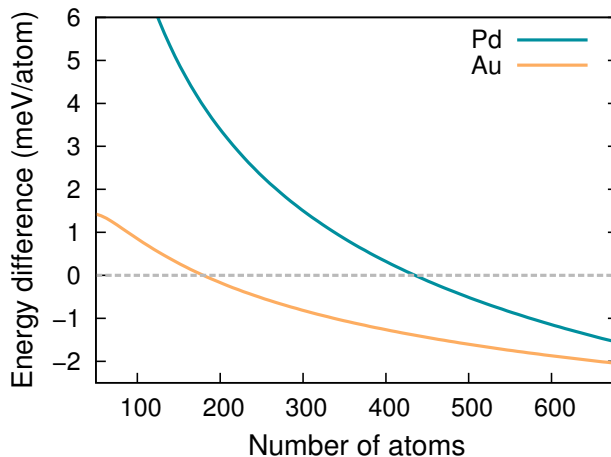


Figure 4.11: *Difference between energy per atom in regular truncated octahedra and icosahedra. Positive and negative values imply that icosahedra and regular truncated octahedra are energetically favourable, respectively.*

4.5 An algorithm for the determination of optimal particle shapes

As already mentioned, an icosahedron or a regular truncated octahedron cannot be created with any number of atoms. By relaxing the symmetry requirement slightly, one could nevertheless imagine an incredible number of different ways to construct particles similar to icosahedra or regular truncated octahedra. In very much the same way as all configurations of Pd and Au atoms in an alloy span an enormous phase space, all possible nanoparticle shapes span a huge “structural phase space” which we could never sample by brute force. Here, this challenge is attacked with Monte Carlo integration in the variance-constrained semigrand canonical ensemble.

4.5.1 Computational procedure

The method can be described as follows; instead of modeling an alloy of two different species of metal atoms, we change one of the species into “ghost atoms” that do not interact with anything. Clearly, such a system is immiscible – the metal atoms would rather group together than being spread out in empty space. Thus, as described in Chapter 3, the semigrand canonical ensemble cannot be used. Instead, we may force the system to intermediate concentrations, with the use of the variance-constrained semigrand canonical ensemble. In this way, we can sample many different shapes in an efficient search for optimal nanoparticles with any number of atoms.

A growth simulation is carried out as follows:

1. A simulation box with non-periodic boundary conditions is defined and filled with an fcc lattice.
2. In the center of the simulation cell, a small core of Pd or Au atoms is created. Then all lattice sites having at least one but not more than 30 Pd/Au atoms within a distance of 5 Å are made “active”, while all the other sites are

“inactive”. In practice, this means that the atoms close to the surface of the particle are active, as well as the ghost atoms closest to the particle.

3. The VC-SGC parameters $\bar{\phi}$ and $\bar{\kappa}$ are defined and a Monte Carlo run is done:
 - Particle swaps, corresponding to particle insertion and deletion, are performed among the active sites, and a trial swap from “ghost” to “metal” or vice versa is made with a probability given by

$$\min \left\{ 1, \exp \left[-\beta \left(\Delta E + \bar{\kappa} N_{\text{tot}} \Delta c \left(\bar{\phi} + \Delta c + 2c \right) \right) \right] \right\},$$

as described in Chapter 3.

- After N trial swaps an MD step is carried out thermostated to a temperature T_{MD} . The active region is updated and the procedure is repeated.

In these runs, $\bar{\phi}$ was initially set to -2.0 and then subsequently increased in steps of 10^{-4} until the particle had grown to the edge of the simulation box. 2000 MC cycles were performed for each value of $\bar{\phi}$. The constraining parameter $\kappa = \beta \bar{\kappa}$ was set to 10^4 (κ as opposed to $\bar{\kappa}$ has the advantage of being temperature independent). It should be made clear that this algorithm contains two different temperatures, a Monte Carlo temperature T_{MC} that enters in $\beta = 1/k_{\text{B}}T_{\text{MC}}$, and a Molecular Dynamics temperature T_{MD} that allows for atomic relaxation. T_{MC} has to be large, on the order of 1000 K, to achieve a decent acceptance probability, while T_{MD} has to be very small, on the order of nanokelvins, to avoid lattice distortion.

Figure 4.12 shows snapshots from a run for Au. Note that the structures resemble the structures in Fig. 4.7, even though the present ones are less symmetric and do not correspond to “magic numbers”.

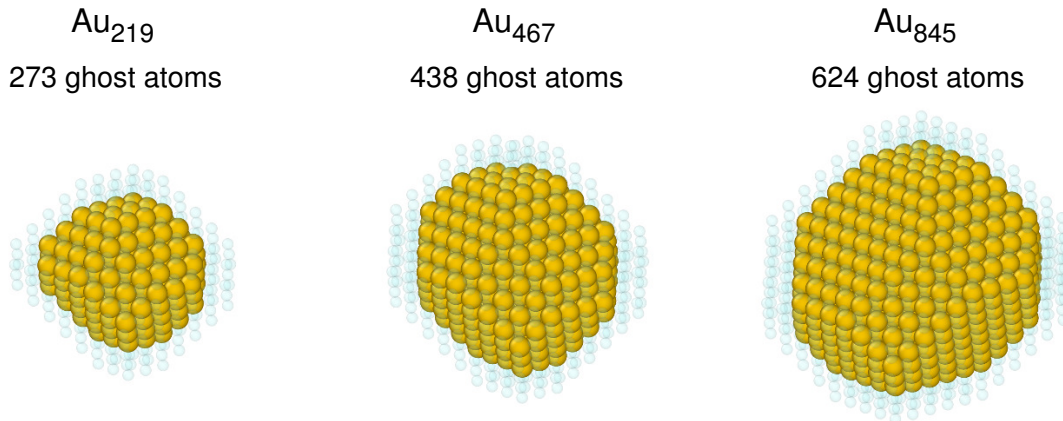


Figure 4.12: Snapshots from a particle growth run in the VC-SGC ensemble, using Au. The transparent blue atoms are the active “ghost atoms”.

4.5.2 Results

The algorithm has been applied to pure Pd and Au, using the same EAM potential that was used for the alloy simulations. Figure 4.13 shows energy per atom relative to the fits of the regular truncated octahedra data described above, for Pd and Au respectively, as obtained with the particle growth method. The plots are constructed out of four runs with different random seeds, and for each number of atoms, the run

with the lowest energy was chosen for Fig. 4.13. Note that most regular truncated octahedra are found in at least one of the four runs. Further, these regular truncated octahedra are indeed among the structures with lowest energy. What is perhaps most striking is that already for fairly small particles, the energy landscape is quite flat; the energy penalty of creating a particle that is not fully symmetric is low, less than 5 meV per atom compared to the limit representing regular truncated octahedra. From an experimental perspective, we can thus not expect the size distribution of an ensemble of nanoparticles to be too localized around certain magic numbers, but rather fairly polydisperse (even though such a property is highly dependent on kinetics).

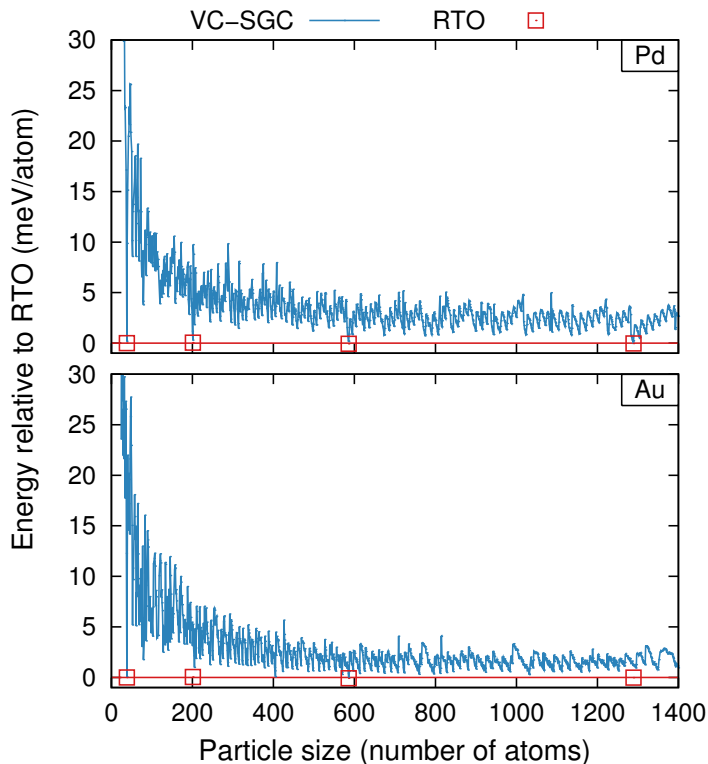


Figure 4.13: Energy per atom for structures as obtained with the particle growth method in the VC-SGC ensemble in a perfect fcc lattice at $T_{MC} = 1000$ K and $T_{MD} = 10$ nK. The energies are the lowest values obtained out of four different runs. Energy is measured relative to a fit of the red squares, representing the energies of regular truncated octahedra.

The small temperature $T_{MD} = 10$ nK is not enough to overcome the energy barrier separating truncated octahedra and icosahedra. To investigate the icosahedral energy landscape, particle growth simulations were also carried out in which the underlying lattice represented a large icosahedron, rather than a perfect fcc lattice. The results are shown in Fig. 4.14. For Pd, the icosahedral shape is preserved, and all magic number icosahedra are visited. For Au, however, the particle gets distorted and ends up sampling low-symmetry clusters at much higher energies. By turning off the temperature completely, the icosahedral shape is retained, and the system finds the low-energetic shapes. It does, however, end up slightly above the red squares in Fig. 4.14d. The reason is that the clusters are not allowed to relax since the MD

temperature is zero. The higher energy is thus a consequence of the lattice of these metallic nanoparticles being more and more compressed with decreasing size due to surface stress, as explained in e.g., Ref. 28.

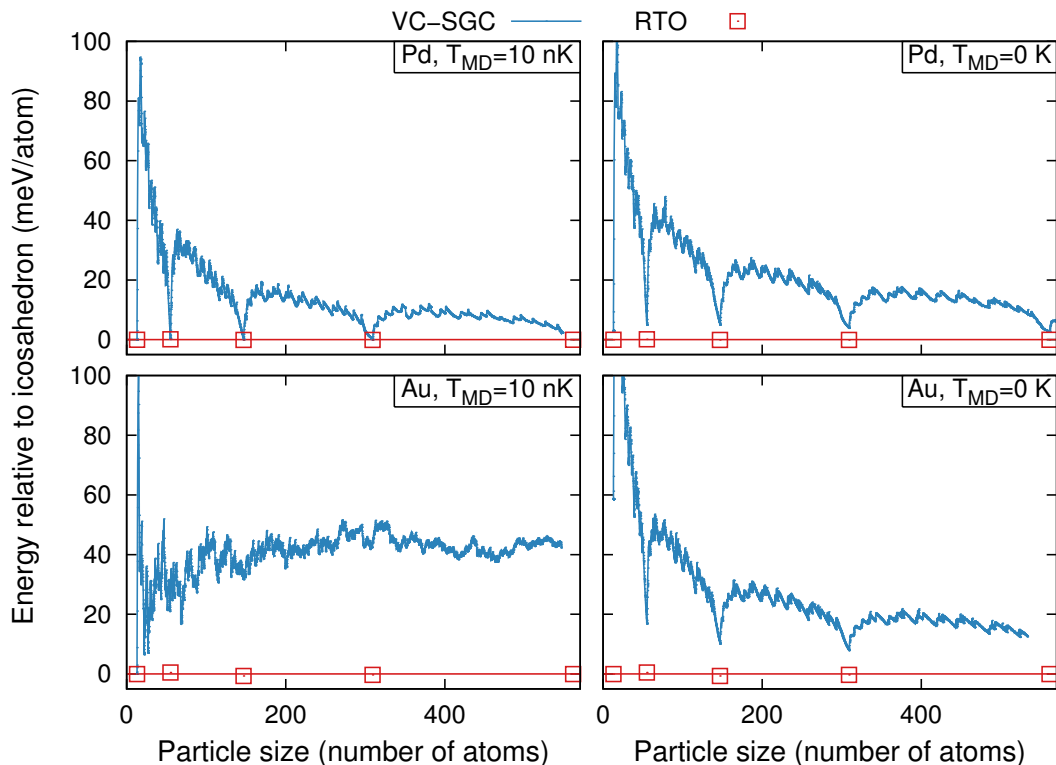


Figure 4.14: Energy per atom for icosahedral structures as obtained with the particle growth method in the VC-SGC ensemble. Energy is measured relative to a fit of the red squares, representing energy for complete icosahedra.

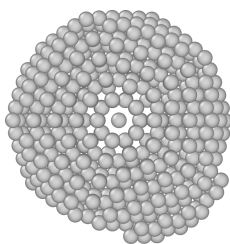


Figure 4.15: Snapshot from particle growth run with Pd in an icosahedral lattice. The first atoms in the next shell stick out in the lower right corner.

It is interesting to note that structures in between magic icosahedra are associated with a much higher energy penalty than in Fig. 4.13, where a perfect fcc lattice was used. The barriers should be understood as the excess energies of having an incomplete shell surrounding the particle. This is depicted in Fig. 4.15, where an incomplete shell sticks out from the particle in the lower right corner. Creating an incomplete shell is inevitably associated with highly energetic steps on the surface. The situation can be compared to particles obtained on a perfect fcc lattice, for

instance those in Fig. 4.12, where the particle may retain a rounded, stepless shape, by getting slightly elongated. The size distribution of an ensemble of icosahedral particles can thus be expected to be more localized at the magic numbers.

4.6 Pd-Au nanoparticles

The computational method used for bulk and surface systems is now directed towards some low-energetic particle shapes identified in Section 4.4. The focus will be on regular truncated octahedra and icosahedra comprising less than about 1300 atoms, corresponding to diameters of less than roughly 3 nm.

Figure 4.16 shows the chemical potential difference as a function of concentration for icosahedra and regular truncated octahedra for sizes up to 1289 atoms. For the smallest clusters, we can easily identify regions where the slope is very large, indicating ordered configurations. For larger particles, however, the picture is less clear – the curves become more and more featureless.

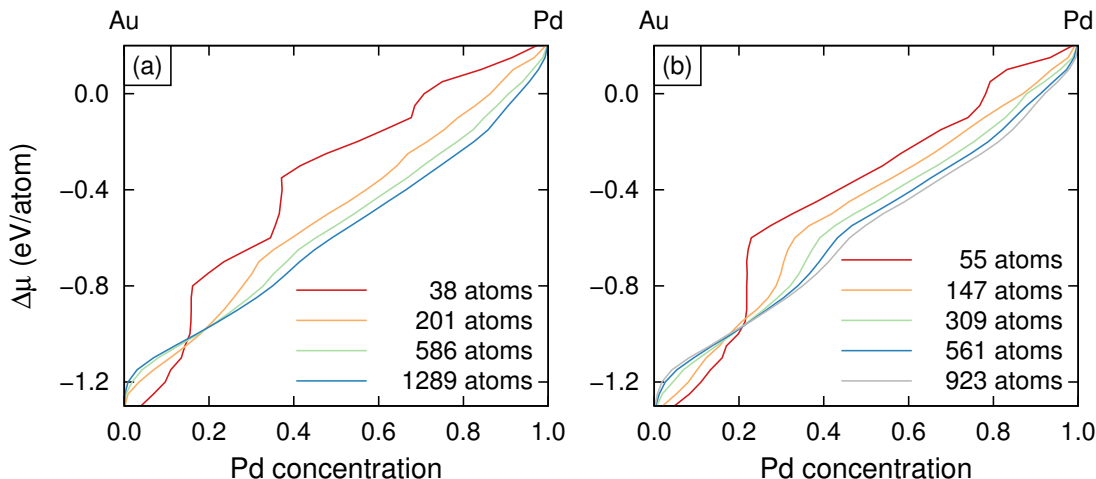


Figure 4.16: Chemical potential difference versus concentration at 300 K for (a) regular truncated octahedra and (b) icosahedra.

From studying the trajectories of the small particles, it becomes clear that the system adopts certain ordered configurations in the vertical intervals. These configurations are shown in Fig. 4.17 for the 38 atom regular truncated octahedron and the 55 atom icosahedron. Note that they are consistent with the predictions from the surface calculations with excess Au on the surface, and if the surface is not completely Au, there are structures reminiscent of the honeycomb patterns in Fig. 4.5.

For larger particles, the trajectories do not immediately reveal any clear preferred configurations. Nevertheless, some sites are of course more likely to be occupied by Au and some by Pd. This situation can be quantified by measuring the number of snapshots a certain site is occupied by an Au atom compared to the total number of timesteps (at a certain $\Delta\mu$). The result is visualized in Fig. 4.18 for regular truncated octahedra with 201, 586 and 1289 atoms. Note that there is always more Au on the surface than elsewhere in the particle, and that there is always more

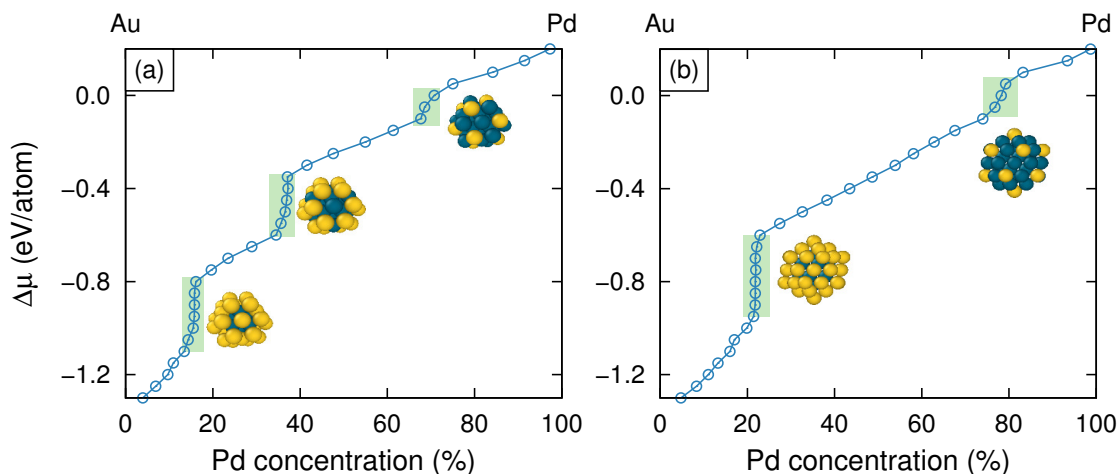


Figure 4.17: Chemical potential difference versus concentration at 300 K for (a) 38 atom regular truncated octahedron and (b) 55 atom icosahedron. The green rectangles indicate the vertical regions, corresponding to the ordered configurations shown besides.

Pd underneath the surface. Further, corner and edge sites are particularly likely to be Au, an observation that might be of importance in e.g., catalysis.

4.6.1 Annealing

One of the aims of this thesis is to examine the impact of order on the plasmonic properties of nanoalloys. To this end, particles that are both ordered and thermodynamically stable are particularly interesting. The indefiniteness of some of the atoms in large particles, manifested by gray atoms in Fig. 4.18, prevents us from finding such particles by just looking at the trajectories. As was shown in Section 4.2, however, lower temperatures may reveal ordered configurations. Would it be a good idea to run the Monte Carlo simulations at lower temperature? The problem with doing so is that the acceptance probability might be so low that the sampling becomes inefficient and the relevant configurations are missed.

To overcome this problem, simulations were run in what may be described as an annealing procedure. Simulations were started at 500 K, where the acceptance probability is quite high, and then the temperature was lowered in steps of 5 K, to 20 K. 30 000 MD timesteps were run at each temperature. The chemical potential difference $\Delta\mu$ was kept fixed throughout the annealing. In principle, this should freeze the particle into a configuration obtained without bias towards a chosen initial configuration.

This method has previously been used to map the size-dependent phase diagrams of Pt-Rh nanoparticles [29]. The Pt-Rh simulations suggested that the system never ends up at certain concentrations at low temperatures, regardless of $\Delta\mu$, but instead forms certain ordered phases. Figure 4.19 shows an attempt to a similar analysis with a 201 atoms regular truncated octahedron of Pd-Au. Some concentrations attract trajectories from a fairly wide range of $\Delta\mu$ values, but perhaps not strong enough to talk about “phases” in the strict sense. Still, the “attracting concentrations” turn out to very often be highly symmetric, usually retaining

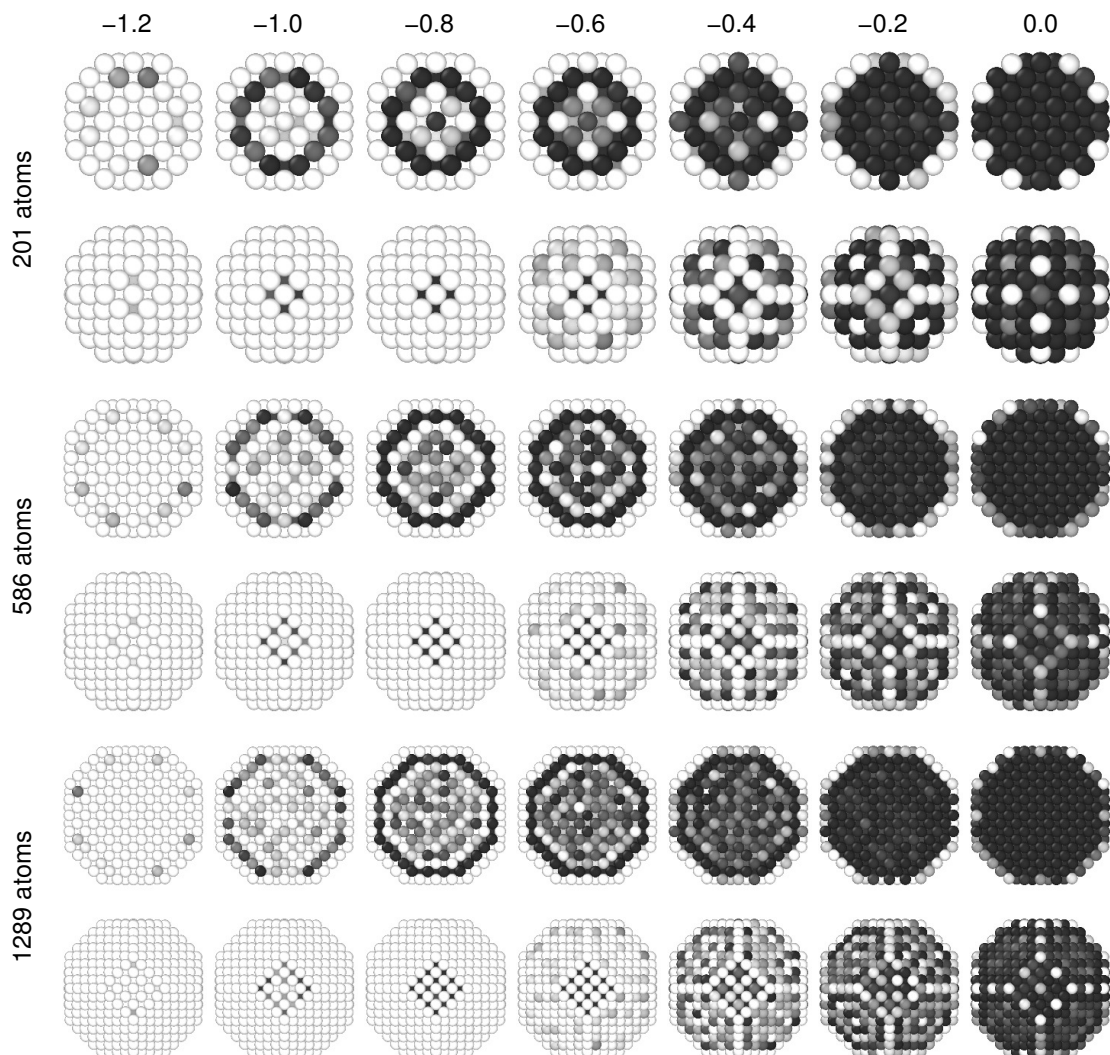


Figure 4.18: Average concentration at each site in regular truncated octahedra of different sizes, for $\Delta\mu$ ranging from -1.2 to 0.0 eV/atom. White means 100 % Au, and black 100 % Pd. Each particle is showed from above (lower) and sliced thorough its center (upper).

the octahedral symmetry. Figure 4.20 shows four structures that were found to be particularly stable.

4.6.2 Verification of the potential

The results presented in this chapter are entirely dependent on the accuracy of the EAM potential. This issue may be addressed by comparing the mixing energy in Pd-Au nanoparticles as obtained with the EAM potential and with DFT, in this case the PBE exchange-correlation functional and an atomic orbital basis set (for details, see the next chapter). The results are presented in Fig. 4.21. The potential seems to overestimate the mixing energy slightly, as was seen also in the bulk case. Note also that the potential overestimates the mixing energy more for the ordered configurations than random ones, indicating that the potential may make

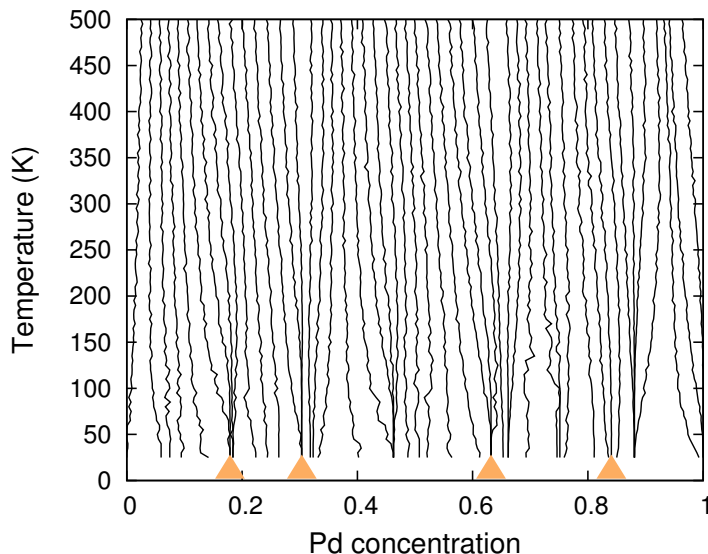


Figure 4.19: Trajectories from annealing in the semigrand canonical ensemble. The lines correspond to annealing at different fixed $\Delta\mu$. The orange triangles indicate the positions of ordered particles shown in Fig. 4.20.

the nanoparticles too prone to attain ordered structures compared to PBE-DFT.

4.7 Summary

The most important results with implications for the calculation or interpretation of optical properties of Pd-Au nanoparticles can be summarized as follows:

- Au segregates to the surface, in particular to corner and edge sites;
- The subsurface layer has excess of Pd, and the distribution of Pd and Au becomes homogeneous further into the core;
- The icosahedral shape is lower in energy than truncated octahedra for small particles (less than a few hundred atoms), while the situation is reversed for large particles;
- Highly symmetric particles come in certain magic numbers, but the energy landscape between the particles is quite flat if the symmetry requirement is relaxed;
- For small particles ($\lesssim 100$ atoms), ordered configurations can easily be found all the way up to room temperature. For larger particles ($\gtrsim 100$ atoms) lower temperatures are needed.

If LSPR is indeed a surface phenomenon, the composition of the surface should be of outstanding importance. Thus, the by far most important result from this chapter is the segregation of Au to the surface.

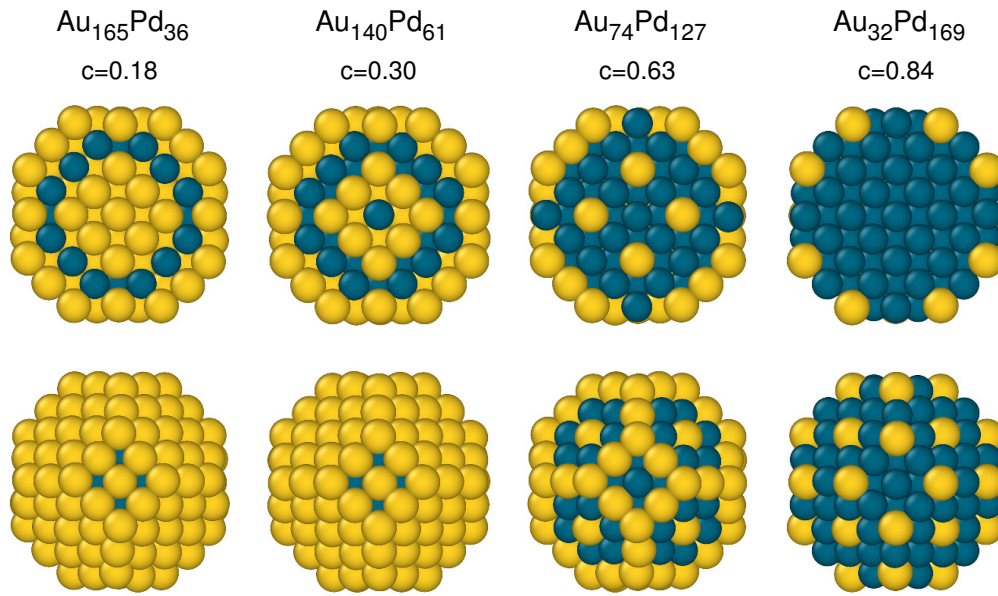


Figure 4.20: Ordered structures found by annealing 201 atom regular truncated octahedra, sliced through center (upper row) and seen from above (lower). The labels indicate chemical composition and concentration of Pd.

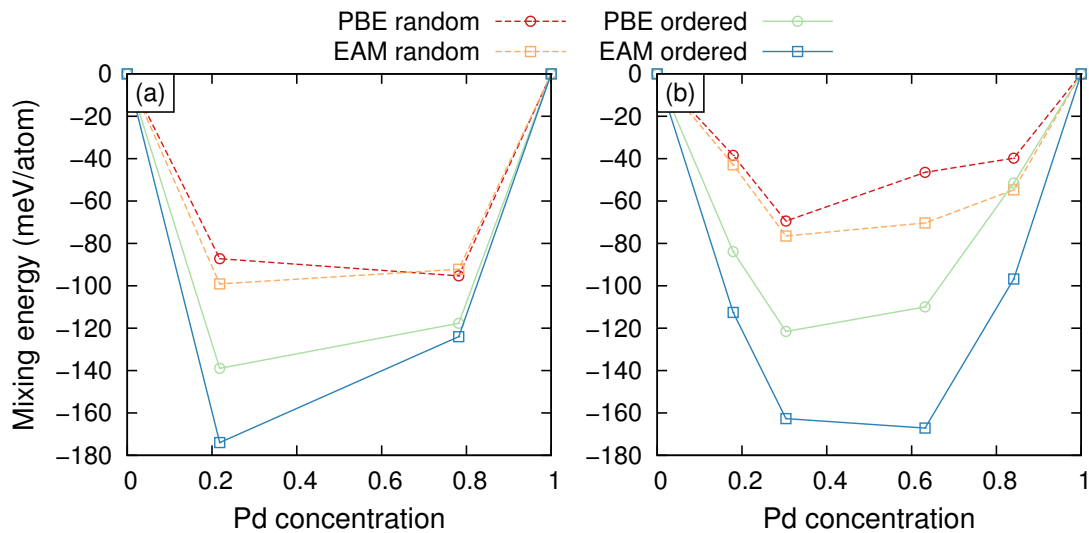


Figure 4.21: Potential energy of mixing for (a) 55 atom icosahedron and (b) 201 atom regular truncated octahedron as obtained with the EAM potential and with DFT using the PBE exchange-correlation functional and an atomic orbital basis set.

5

Optical response of Pd-Au nanoparticles

The optical response of any material is closely related to the electronic structure. Classical atomistic calculations, as those presented in the previous chapter, are thus insufficient for elucidating the plasmonic properties of Pd-Au nanoparticles. This chapter presents the results of first-principles calculations on some of the thermodynamically stable Pd-Au nanoparticles described in the previous chapter as well as Pd and Au in bulk.

The calculations can be divided into two major parts, (time-independent) density functional theory (DFT) and time-dependent density functional theory (TDDFT). The former yields the ground state of the system, providing important information such as the density of states. The ground state wavefunction is also used to initialize TDDFT calculations, where the system is subject to a sudden electromagnetic kick, after which the electronic structure is allowed to propagate in time, revealing the optical response of the particle. All calculations presented here were performed in the GPAW code [30, 31].

5.1 Electronic structure in bulk

Even though nanoparticles have electronic properties that differ significantly from the bulk, there is of course some correlation between the two. To get some preliminary insights, bulk calculations were carried out for pure Pd and Au. The setup consisted of one atom and periodic boundary conditions. The Brillouin zone of the primitive cell was sampled with 20 \mathbf{k} -points in each direction and a plane wave basis set with a cutoff energy of 400 eV was used. Two exchange-correlation functionals based on the generalized gradient approximation (GGA) were employed, PBE [26] and GLLBSC [32, 33]. The lattice parameter was chosen by running multiple calculations with the PBE functional and finding the minimum in energy, which turned out to be 3.940 Å for Pd and 4.173 Å for Au.

The resulting band structure and density of states are shown in Fig. 5.1. As was briefly mentioned in Chapter 2, the nature of the plasmon peak is highly dependent on its energy compared to the distance between the Fermi level and the d -band. From Fig. 5.1 we note that Pd and Au are fundamentally different with respect to the position of the d -band. While the upper edge of the d -band of Pd lies at the Fermi level, so that d electrons can be excited to s and p states already for very low energies, there is a distance of about 2 eV from the d -band edge to the Fermi level

5. Optical response of Pd-Au nanoparticles

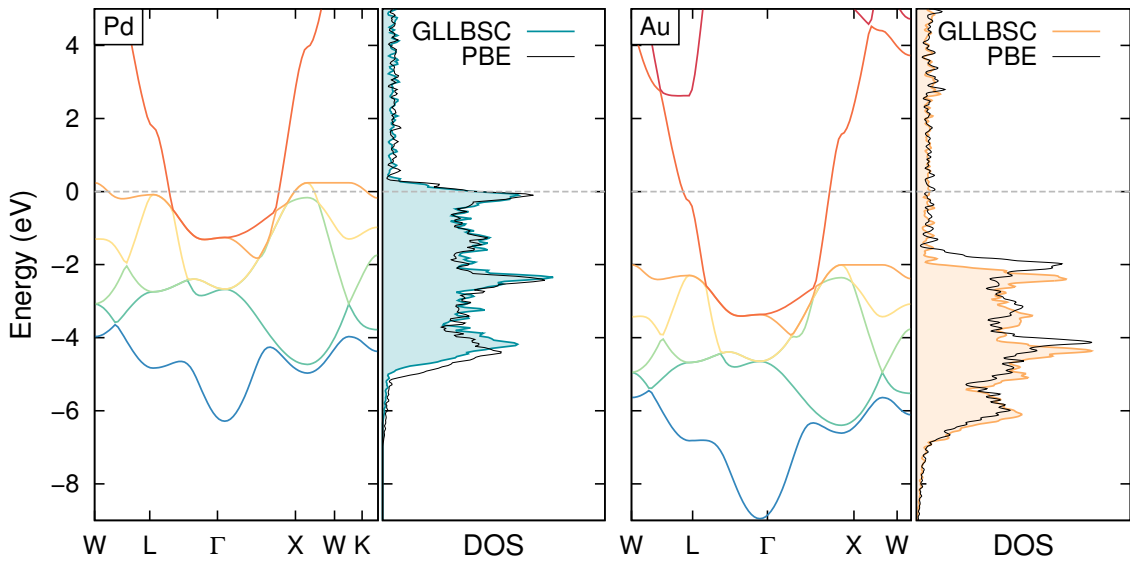


Figure 5.1: Band structure of Pd and Au in bulk, and corresponding density of states. The band structures were obtained with the GLLBSC functional, but the density of states is shown for both GLLBSC and PBE. The energies are measured relative to the Fermi levels (marked with the dashed gray line).

for Au. This is consistent with the observations made in connection to the dielectric function in Chapter 2. This paves the way for a sharper plasmon peak in Au as compared to Pd, provided that it is lower in energy than about 2-3 eV.

The PBE and GLLBSC functionals give very similar results. Notice, however, that the d -band for Au is shifted between the two functionals. In particular, the distance between the d -band edge and the Fermi level is about 0.3 eV larger with the GLLBSC functional. In this respect, the GLLBSC functional agrees better with experiment, at least for Au [5].

5.1.1 Lattice parameter

It is a well-known fact that PBE tends to overestimate the lattice parameter. Indeed, the lattice parameters obtained with PBE (3.940 Å for Pd and 4.173 Å for Au) are larger than experimental values (3.89 and 4.08 Å [25]). Since the structures were relaxed with PBE, the particles can be expected to be slightly larger than what they would have been in real life. This does of course have some impact on the calculated absorption spectra. Figure 5.2 shows the density of states calculated with different lattice parameters. Making the lattice parameter smaller broadens the d -band slightly, but the shape remains the same, and more importantly the upper edge stays in the same place. It thus seems unlikely that the overestimation of the lattice parameter has a large impact on the absorption spectra.

5.2 Computational approach to nanoparticles

When going from bulk to nanoparticles, the DFT approach has to be changed slightly. The plane wave basis set used for bulk requires a periodic system and is thus not optimal for a finite system. For nanoparticles, an atomic orbital basis set

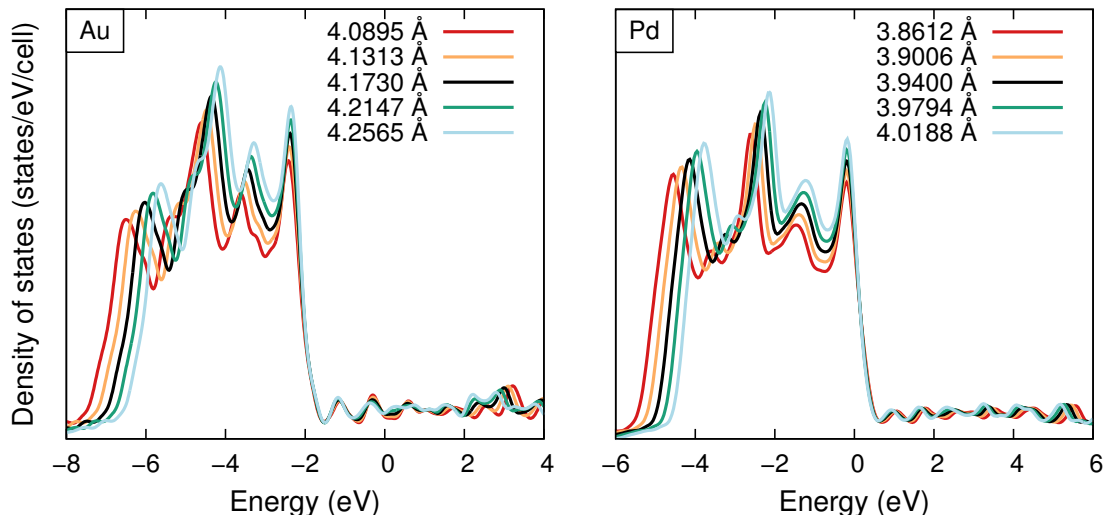


Figure 5.2: Density of states of Au and Pd in bulk, relative to the Fermi level, for different lattice parameters, calculated with the GLLBSC functional. The black lines represent the equilibrium lattice parameter as obtained with PBE. For clarity, the lines are smoothed compared to Fig. 5.1.

is more suitable. Linear combination of atomic orbitals (LCAO) in time-propagation TDDFT mode has recently been implemented in GPAW [21]. The computational efficiency is very sensitive to the choice of basis set. For TDDFT calculations, this is perhaps even more crucial since electrons may get excited to otherwise unoccupied orbitals. The basis sets are constructed as products of radial functions and spherical harmonics [34],

$$\varphi_{nlm}(\mathbf{r}) = R_{nl}(r)Y_{lm}(\hat{\mathbf{r}}). \quad (5.1)$$

In the present calculations, two radial functions $R_{nl}(r)$ were included for each (nl) . The basis functions should correspond to the valence states of the atoms and, in addition to the highest occupied states, the lowest unoccupied states need to be included. For Pd this means that there will be two radial functions each for $4d$, $5s$ and $5p$, and for Au two each for $5d$, $6s$ and $6p$. Each level (nl) comes with $2l+1$ spherical harmonics, meaning that there are $2 \cdot 1 + 2 \cdot 3 + 2 \cdot 5 = 18$ basis functions $\varphi_{nlm}(\mathbf{r})$ for each atom. This can be compared to dividing the computational regime into a grid, in which case 18 grid points “per atom” would be equivalent to a grid spacing of roughly 1 \AA , which represents a very coarse grid (suitable values are typically about 0.2 \AA and below). LCAO can thus speed up the computations significantly, but the results will be dependent on the quality of the basis set. Figure 5.3 compares the density of states of pure Pd and Au as 55 atom icosahedra obtained with LCAO and grid-based calculations with the grid spacing 0.3 \AA . The densities are in good agreement, suggesting that the basis set provides a sufficiently accurate description.

The Hamiltonian matrix is still computed on a real space grid and to this end a grid spacing 3.0 \AA was used. A vacuum region of 5 \AA between the atom cores and the simulation cell box face was used. Making the grid spacing denser and adding more vacuum had no significant impact on the results.

Near the Fermi level, the eigenenergies are degenerate or close to being degenerate, and in order to converge the self-consistency loop the occupations have to be

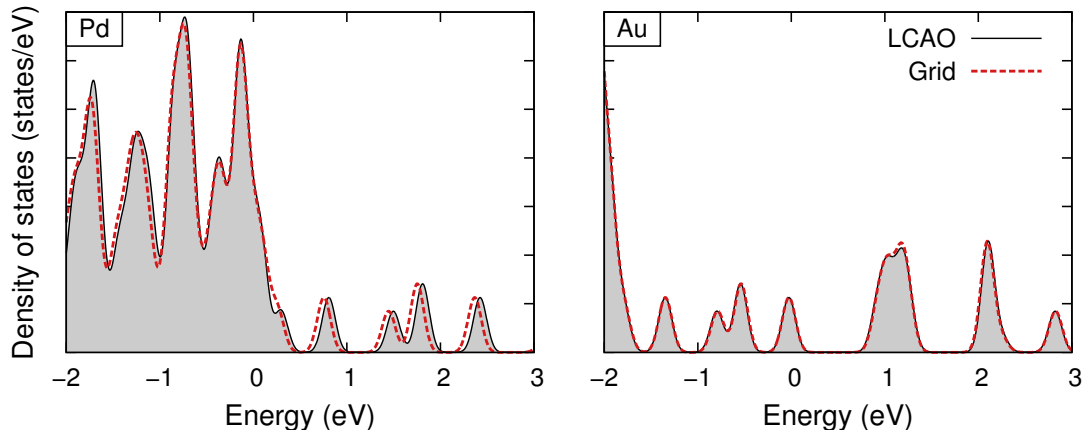


Figure 5.3: Density of states close to the Fermi level in icosahedral Pd_{55} and Au_{55} , as obtained with LCAO and grid-based calculations.

smearred. Here, Fermi-Dirac smearing with a temperature of 0.05 eV was used. The GLLBSC functional was employed in all calculations, unless stated otherwise. The TDDFT calculations were propagated for 2000 timesteps of 10 as each. A shorter timestep or longer propagation had no significant impact on the absorption spectra.

5.3 The 55 atom icosahedron

DFT and TDDFT calculations were performed on six different 55 atoms icosahedra identified in Chapter 4; pure Pd, pure Au, the football-ordered $Au_{12}Pd_{43}$ and onion-ordered $Au_{43}Pd_{12}$ (shown in Fig. 4.17), as well as randomly ordered icosahedra with the same concentrations as the latter two. The density of states for these particles, as obtained with DFT, is shown in Fig. 5.4. Note that the position of the d -band in the pure clusters is similar to that in the bulk. The clusters with intermediate concentrations exhibit intermediate behavior, with the d -band shifting from the Au position to the Pd position as the concentration of Pd is increased. Further, note that the clusters with random configuration have a more smearred density of states compared to the ordered ones. This is not entirely surprising, since a random cluster is likely to have 55 unique atoms, while many atoms are equivalent by symmetry in an ordered cluster. Where many atoms are equivalent, there will also be many equivalent states, thus collectively building up major peaks in the density of states. These peaks will be smearred when the atoms have different neighbors, as in the case of the random cluster.

Absorption spectra obtained with TDDFT are shown in Fig. 5.5. The spectra have many peaks, but one should not at this point ascribe these to plasmonic behavior as they might as well be related to single-particle excitations. Indeed, between 2 and 3 eV where the Au plasmon peak is expected to emerge, there is very little absorption. The non-existence of a plasmon peak in Au_{55} is consistent with previous work [35]. Note that the smearred impression of the random clusters as compared to the ordered structures, is exhibited also in the absorption spectrum. Figure 5.5 also contains absorption spectra for Au_{55} and Pd_{55} obtained with the PBE functional. Note that they are very different from the GLLBSC results, highlighting the fact that the exchange-correlation functional has to be chosen carefully.

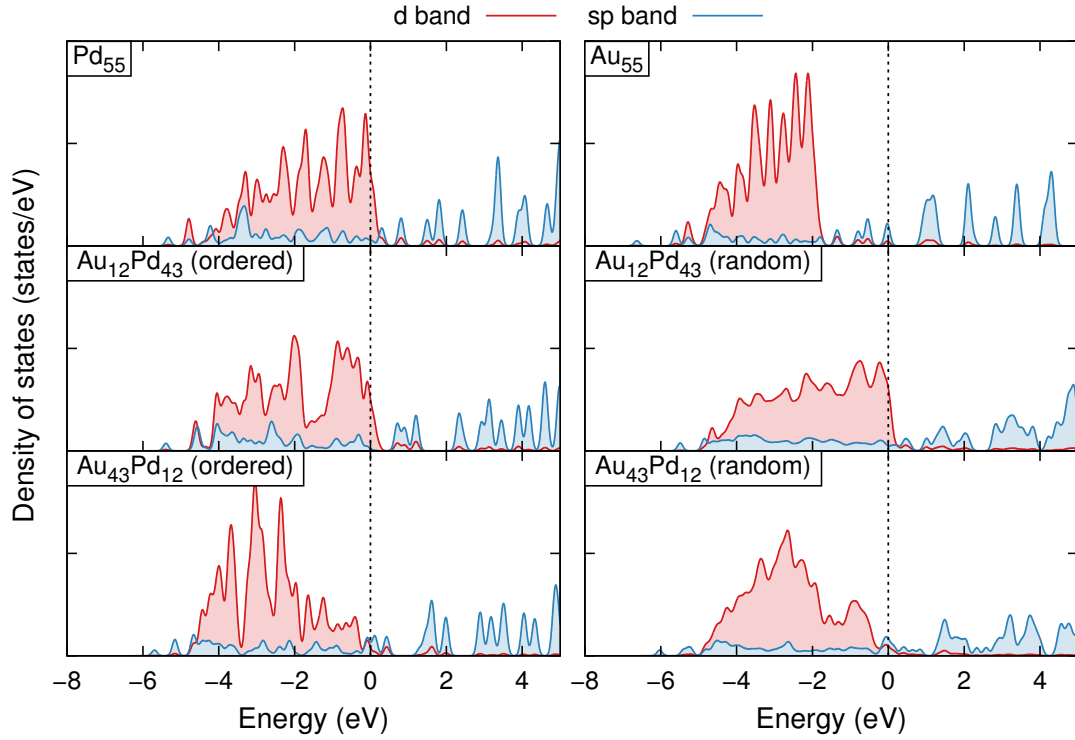


Figure 5.4: Density of states for 55 atom icosahedra with different concentrations, representing ordered as well as randomized elemental distributions. Energy scale is relative to the respective Fermi level, marked with the dotted black line.

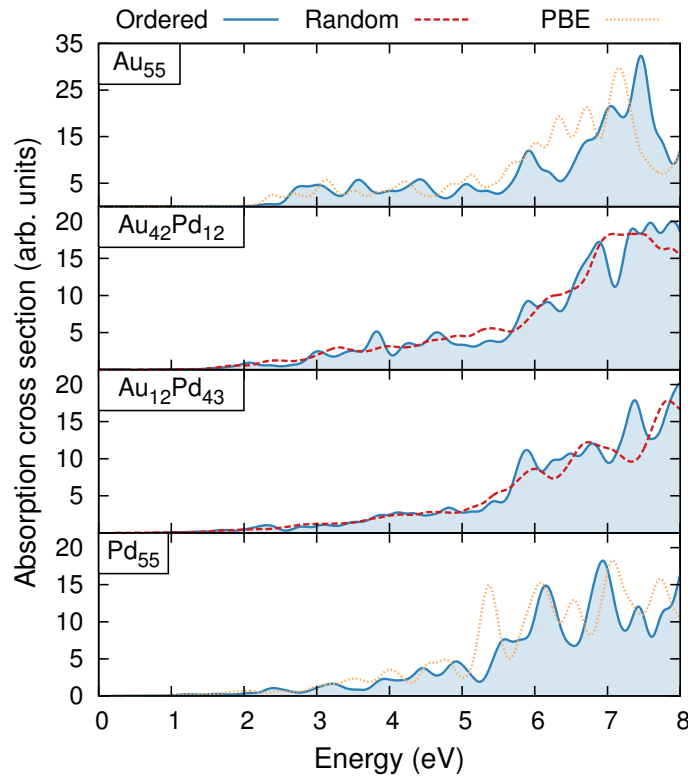


Figure 5.5: Absorption spectra for 55 atom icosahedra. The blue and red lines, corresponding to ordered and randomly distributed clusters, were obtained with the GLLBSC functional.

5.4 The 201 atom regular truncated octahedron

DFT as well as TDDFT calculations with 201 atom regular truncated octahedra (RTO) were carried out using pure Pd, pure Au, and the four structures shown in Fig. 4.20, as well as randomly ordered RTOs with the same concentrations. The $\text{Au}_{32}\text{Pd}_{169}$ system did not converge in the ground state calculations and is therefore excluded in what follows.

The resulting densities of states are shown in Fig. 5.6. They are similar to the densities in 55 atoms icosahedra but less concentrated to individual peaks, thus looking more similar to the bulk density of states.

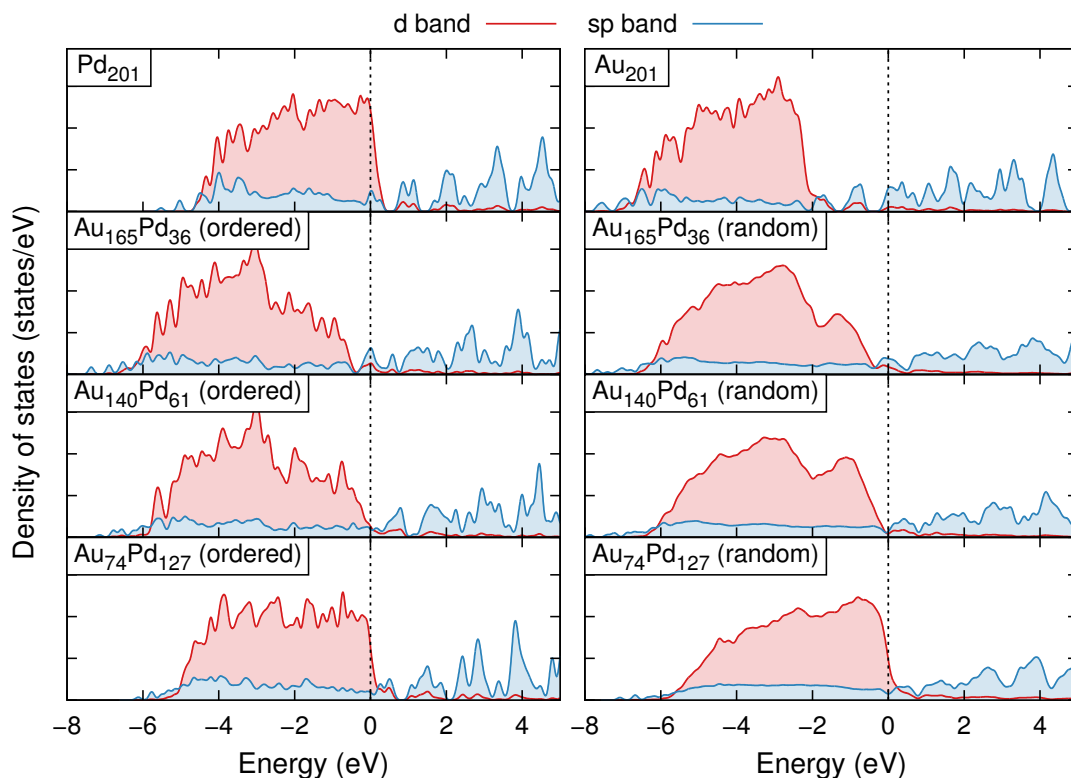


Figure 5.6: Density of states for 201 atoms regular truncated octahedra with different concentrations, ordered and in random configuration. Energy scale is relative to the respective Fermi level, marked with the dotted black.

Figure 5.7 shows absorption spectra obtained for the 201 atom RTOs. Unfortunately, they do not reveal much structure. What were believed to be single-particle excitations in the 55 atom icosahedron spectrum, are now smeared out into a more or less continuous spectrum, similar for all concentrations. It is apparent that these absorption spectra alone are not sufficient for explaining any phenomena related to LSPR.

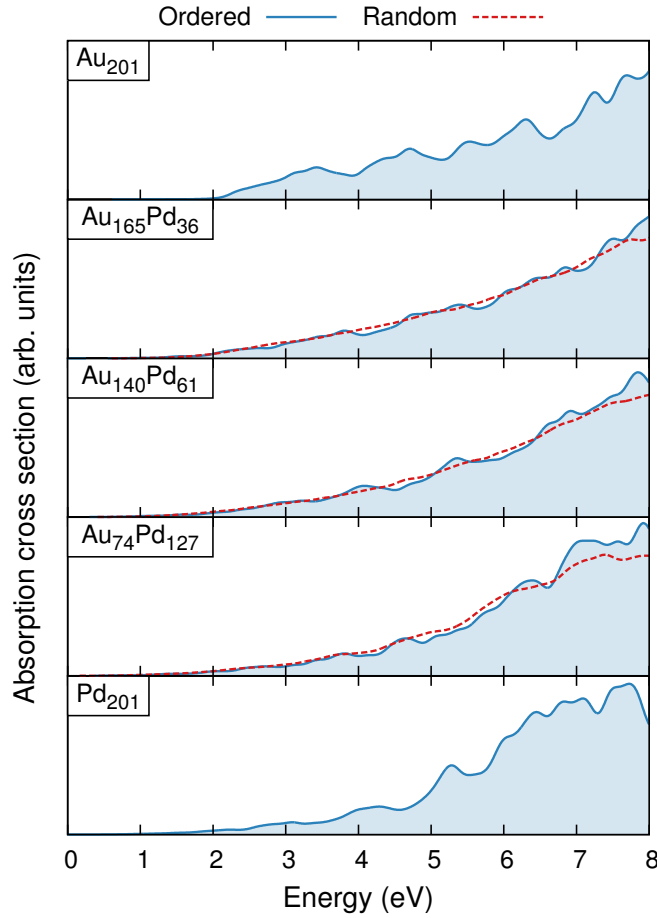


Figure 5.7: Absorption spectra for 201 atom regular truncated octahedra.

5.4.1 Induced density

It is instructive to visualize the induced electron density in the particle. To do so, we may consider the Fourier transform of the time-dependent density $n(\mathbf{r}, t)$,

$$\hat{n}(\mathbf{r}, \omega) = \int_0^{t_{\max}} [n(\mathbf{r}, t) - n(\mathbf{r}, 0)] e^{i\omega t} e^{-\eta t} dt \quad (5.2)$$

where $n(\mathbf{r}, t)$ is recorded throughout the TDDFT run from $t = 0$ to t_{\max} . The factor $e^{-\eta t}$ is a window function serving to suppress the frequency components that enter from the sudden cutoff at t_{\max} . The result is visualized in Fig. 5.8 for Pd_{201} and Au_{201} . Obviously, the charge is very much localized at the surface. This is not surprising; it is a well-known result from electrostatics that free charges in a conductor will end up at the surface to screen the electric field within the conductor. Note, however, that there is some pronounced charge oscillations also in the interior of the particle, especially at high frequencies. This is not expected from a strict application of the free electron model. These oscillations are essentially oriented in the opposite direction compared to the charge oscillations on the surface, and thus act to screen the field originating from there.

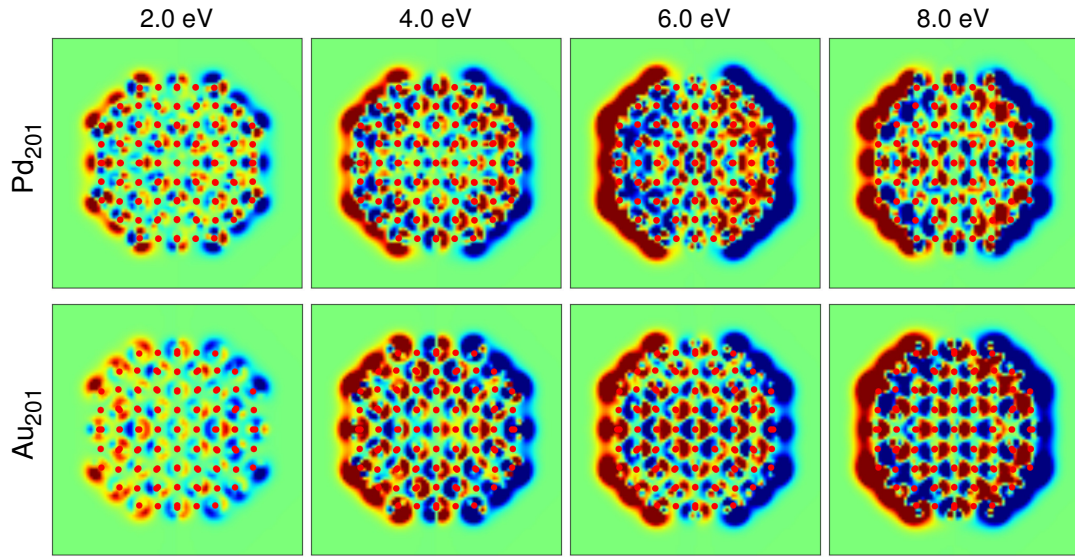


Figure 5.8: Imaginary part of Fourier transform of induced density in Pd₂₀₁ and Au₂₀₁ (RTO) at frequencies corresponding to 2, 4, 6 and 8 eV. The systems were kicked along the horizontal axis, and the images represent the induced density at a cross-section through the center of the particle. Atomic positions are indicated by red circles.

5.4.2 The atomic density matrix

The usage of atomic orbitals as basis set for the TDDFT calculations provides a natural way of decomposing the absorption spectrum for further analysis. From an atomic orbital point of view, the oscillation of the dipole moment is a result of the electrons oscillating between different orbitals, leading to variations in the dipole moment over time. The atomic density matrix

$$D_{l_1 l_2}^a = \sum_i f_i \langle \tilde{p}_{l_1}^a | \tilde{\psi}_i \rangle \langle \tilde{\psi}_i | \tilde{p}_{l_2}^a \rangle \quad (5.3)$$

contains much of the information of interest. Here, a is an atom index, so that we have one matrix $D_{l_1 l_2}$ for each atom in the system. The indices l_1 and l_2 refer to the basis states with corresponding projector function \tilde{p} , and $\tilde{\psi}_i$ are the pseudo wave functions, with corresponding occupation f_i .

The matrices $D_{l_1 l_2}^a$ may be used to ascribe the charge oscillations to different transitions. In Chapter 2, the plasmon resonance was derived as the frequency where the free electrons are in resonance with the electric field. In the case of Au, it is the s electrons that should be regarded as free, since energetically they are closest to the Fermi level. Furthermore since the $6p$ level is very close to $6s$, these levels hybridize. Hence, we may treat s and p electrons on an equal footing. Further, in Chapter 2 the d electrons were seen to be more closely related to damping. It is thus likely that any plasmonic excitation in Au will be more striking if the d electrons are neglected. Thus, we sum $D_{l_1 l_2}^a$ into two groups based on the angular momentum quantum numbers,

$$\hat{D}_{sp}^a \equiv \sum_{l_1 \text{ and } l_2 \notin d} \hat{D}_{l_1 l_2}^a \quad \text{and} \quad \hat{D}_d^a \equiv \sum_{l_1 \text{ or } l_2 \in d} \hat{D}_{l_1 l_2}^a \quad (5.4)$$

where \hat{D} denotes the Fourier transformed quantity. Equation (5.4) now enables one to assess the relative importance of the different atoms. Figure 5.9 shows the result for Au_{201} , with (a) and (b) corresponding to \hat{D}_{sp}^a and \hat{D}_d^a respectively. It is once again striking that excitations within the sp -band happen almost exclusively on the surface, and in particular on the surface atoms that are on the end of the particle with respect to the kick direction (the red curves). For d electrons, the excitations are more equally distributed between surface atoms and bulk atoms. It is thus likely that the charge oscillations inside the particle, observed in Fig. 5.8, can be ascribed to d electrons.

It is interesting to note in Fig. 5.10(a) that there is a peak between 2 and 4 eV, which is where the Au plasmon peak is expected to be (as described in Chapter 2). Whether this peak can be characterized as a plasmon is however still an open question.

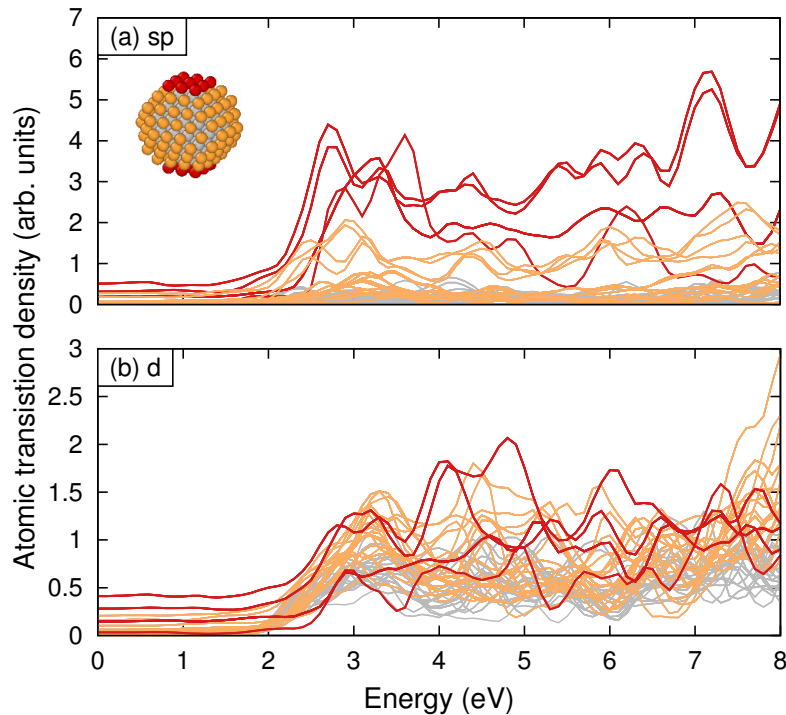


Figure 5.9: Imaginary part of Fourier transform of atomic transition density matrix elements for Au_{201} (RTO). The transition densities are summed over (a) transitions within the sp band, and (b) transitions involving the d band. Each line corresponds to one atom, and the color coding is given by the inset depiction of the particle. The system was kicked in the direction perpendicular to the red faces.

The localization to the surface holds regardless of Pd concentration and ordering. In Fig. 5.10 the quantities \hat{D}_{sp}^a have been summed according to the position of the atom a . This analysis demonstrates that the contribution from atoms in the interior of the particle is very small. Nevertheless, the bulk atoms still have a large impact on what happens in the sp -band. For the ordered $\text{Au}_{165}\text{Pd}_{36}$ and $\text{Au}_{140}\text{Pd}_{61}$ structures, all Pd atoms are in the interior of the particle while the surface consists exclusively of Au atoms. Still, the red curves in Fig. 5.10 differ substantially between these structures and Au_{201} . In particular, note that the plasmon candidate

peaks between 2 and 4 eV die off rapidly. The surface atoms also exhibit a similar behavior for ordered and random particles, even though these surfaces have completely different composition. The subsurface atoms thus have a large impact on the plasmon resonance in Pd-Au nanoparticles, even if the oscillations are localized at the surface. This has previously been observed also in small clusters of Ag-Cu [35] and Ag-Pt [36].

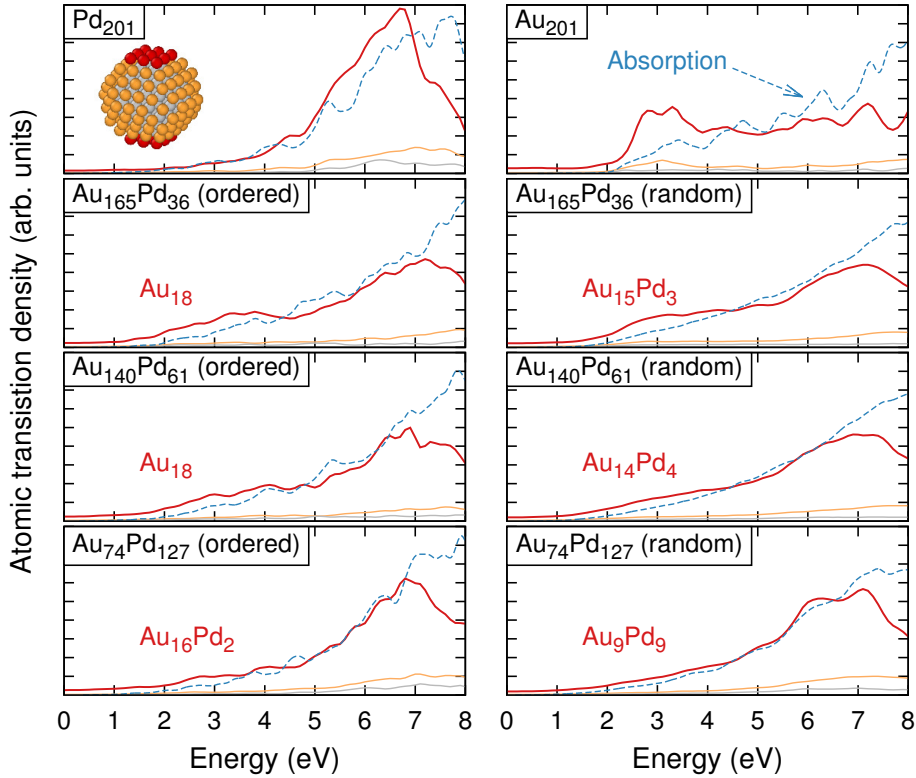


Figure 5.10: Imaginary part of Fourier transform of atomic density matrix elements for 201 atoms RTO, summed over atoms according to the color scheme depicted in the inset. The red labels indicate the composition among the red atoms. The dashed blue lines are the absorption spectra, i.e. the same spectra as in Fig. 5.7, here included for comparison. The curves are normalized by the number of atoms included in the sum. All scales are equal in magnitude.

5.4.3 The plasmonicity index

The plasmonicity index $\tilde{\eta}_P$ described in Section 2.2.2, proposed in Ref. 11 as a tool for characterization of the plasmonic content of absorption peaks, has been evaluated for the Au₂₀₁ and Pd₂₀₁ clusters. The result is shown in Fig. 5.11. At frequencies between roughly 1 and 5 eV, the Au curve is indeed exaggerated compared to the absorption spectrum, but no clear peak can be identified. The plasmonicity index is relatively high also at frequencies where the absorption is low. Against this background, any attempt to discuss plasmonic behavior with basis in the plasmonicity index is doomed to fail. Whether this is a result of the weak plasmons in Au₂₀₁ and Pd₂₀₁ or a shortcoming of the plasmonicity index is a question for the future.

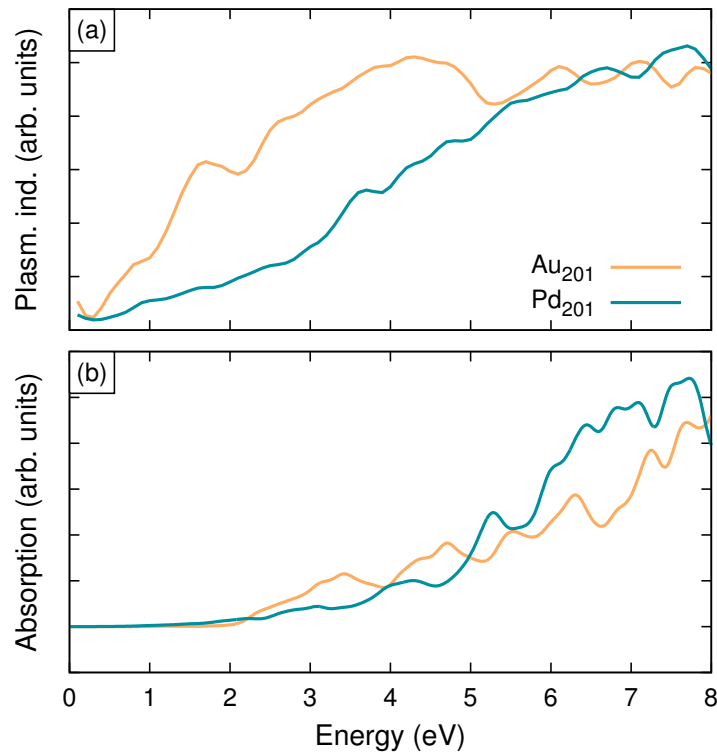


Figure 5.11: (a) Plasmonicity index $\tilde{\eta}_P$ for Au_{201} and Pd_{201} . For comparison, (b) shows the same absorption spectra as in Fig. 5.7.

5.5 Summary

The computations on optical properties of Pd-Au nanoparticles can be summarized as follows:

- The absorption spectra reveal no clear plasmonic peak;
- The analysis tools applied in this thesis are not sufficient to discuss plasmonic behavior in the systems studied here;
- The electronic oscillations are almost exclusively taking place on the surface of the particles, but subsurface atoms still seem to have a substantial impact on the electronic response on the surface;
- Interior atoms play a role in screening of the optical response from excitations in the d -band.

6

Conclusions

In this thesis, atomistic and first principles electronic structure calculations have been carried out to investigate the thermodynamics and optical properties of Pd-Au nanoparticles. The atomistic simulations predicted unambiguously that Au segregates to the surface of the nanoparticles, especially to corner and edge sites. It was also shown using a particle construction algorithm in the variance-constrained semigrand canonical ensemble that, in addition to highly symmetric magic number particles such as icosahedra and regular truncated octahedra, there exist slightly less symmetric low-energetic particles for any number of atoms, as long as the particles are sufficiently large (more than a few hundred atoms). Highly ordered Pd-Au clusters were identified for particle with up to 201 atoms, and these were used for TDDFT calculations of optical properties. The optical absorption spectra for these particles turned out to be quite flat, with no clear plasmon resonances. More elaborate attempts to analyze the results indicated that some plasmonic behavior may be involved, but the results are inconclusive. It was shown that the electronic oscillations to a very high degree take place on the surface of the nanoparticles, but also that interior atoms play an important role, partly in screening by excitations of d electrons, but also in affecting the sp -band at the surface.

The results are not sufficient for making predictions or explain plasmonic properties of Pd-Au nanoparticles. To do so, it would either be necessary to have a distinct plasmon peak in the absorption spectra or a more sophisticated approach to analyze plasmonic content in the current spectra. It should be remembered, however, that no distinct plasmon peak in the visible spectrum can be expected in small, close-to-spherical Pd-Au nanoparticles; the peak is weak also in experimental data [37]. Increasing the size of the particles might reveal some information, but other modifications of the computational setup should be considered as well. As was shown in Chapter 2, the shape of the particles has a profound impact especially on the Au peak. In fact, the Pd-Au experiments [2] motivating this study do not only involve much larger particles, but are actually performed on nanodisks excited along the long axis, thus taking advantage of this shape effect. A distinct plasmon peak has indeed been observed in TDDFT calculations on small Au nanorods [38]. A study of non-spherical particles could even be made thermodynamically well-motivated by conjunction with the particle construction algorithm, which actually predicts elongated particles for some sizes.

The unclear plasmon peak of Pd-Au makes it a troublesome model system for plasmonic response in metallic nanoparticles. For future studies, it might be fruitful to include for instance silver, which exhibits a conspicuous plasmon peak already for very small particles [39]. A system with silver may thus provide a benchmark

6. Conclusions

for the analysis tools, facilitating further studies of Pd-Au.

Bibliography

- [1] Langhammer, C., Zoric, I., Kasemo, B., and Clemens, B. M. (2007) Hydrogen storage in Pd nanodisks characterized with a novel nanoplasmonic sensing scheme. *Nano Letters*, **7**, 3122–3127.
- [2] Wadell, C., Nugroho, F. A. A., Lidström, E., Iandolo, B., Wagner, J. B., and Langhammer, C. (2015) Hysteresis-free nanoplasmonic Pd–Au alloy hydrogen sensors. *Nano Letters*, **15**, 3563–3570.
- [3] Mie, G. (1908) Beiträge zur Optik trüber Medien, speziell kolloidaler Metallösungen. *Ann. Phys.*, **330**, 377–445.
- [4] Johnson, P. B. and Christy, R. W. (1972) Optical Constants of the Noble Metals. *Phys. Rev. B*, **6**, 4370–4379.
- [5] Yan, J., Jacobsen, K. W., and Thygesen, K. S. (2012) Conventional and acoustic surface plasmons on noble metal surfaces: A time-dependent density functional theory study. *Phys. Rev. B*, **86**, 241404.
- [6] Meier, S. A. (2007) *Plasmonics: Fundamentals and Applications*. Springer US, 1 edn.
- [7] Bohren, C. F. and Huffman, D. R. (2007) *Absorption and Scattering of Light by Small Particles*, pp. 130–157. Wiley-VCH Verlag GmbH.
- [8] Sakurai, J. and Napolitano, J. (2011) *Modern Quantum Mechanics*. Pearson, 2 edn.
- [9] Bernadotte, S., Evers, F., and Jacob, C. R. (2013) Plasmons in Molecules. *J. Phys. Chem. C*, **117**, 1863–1878.
- [10] Ma, J., Wang, Z., and Wang, L.-W. (2015) Interplay between plasmon and single-particle excitations in a metal nanocluster. *Nat Commun*, **6**, 10107.
- [11] Bursi, L., Calzolari, A., Corni, S., and Molinari, E. (2016) Quantifying the Plasmonic Character of Optical Excitations in Nanostructures. *ACS Photonics*, **3**, 520–525.
- [12] Pathria, R. K. (1996) *Statistical Mechanics*. Butterworth Heinemann, 2 edn.
- [13] Sadigh, B. and Erhart, P. (2012) Calculation of excess free energies of precipitates via direct thermodynamic integration across phase boundaries. *Phys. Rev. B*, **86**, 134204.

- [14] Sadigh, B., Erhart, P., Stukowski, A., Caro, A., Martinez, E., and Zepeda-Ruiz, L. (2012) Scalable parallel monte carlo algorithm for atomistic simulations of precipitation in alloys. *Phys. Rev. B*, **85**, 184203.
- [15] Metropolis, N., Rosenbluth, A. W., Rosenbluth, M. N., Teller, A. H., and Teller, E. (1953) Equation of state calculations by fast computing machines. *The Journal of Chemical Physics*, **21**, 1087–1092.
- [16] Ullrich, C. A. and Yang, Z.-h. (2014) A Brief Compendium of Time-Dependent Density Functional Theory. *Brazilian Journal of Physics*, **44**, 154–188.
- [17] Hohenberg, P. and Kohn, W. (1964) Inhomogeneous electron gas. *Phys. Rev.*, **136**, B864–B871.
- [18] Kohn, W. and Sham, L. J. (1965) Self-consistent equations including exchange and correlation effects. *Phys. Rev.*, **140**, A1133–A1138.
- [19] Runge, E. and Gross, E. K. U. (1984) Density-functional theory for time-dependent systems. *Phys. Rev. Lett.*, **52**, 997–1000.
- [20] Blöchl, P. E. (1994) Projector augmented-wave method. *Phys. Rev. B*, **50**, 17953–17979.
- [21] Kuisma, M., Sakko, A., Rossi, T. P., Larsen, A. H., Enkovaara, J., Lehtovaara, L., and Rantala, T. T. (2015) Localized surface plasmon resonance in silver nanoparticles: Atomistic first-principles time-dependent density-functional theory calculations. *Phys. Rev. B*, **91**, 115431.
- [22] Plimpton, S. (1995) Fast parallel algorithms for short-range molecular dynamics. *Journal of Computational Physics*, **117**, 1–19, <http://lammps.sandia.gov>.
- [23] Marchal, R., Genest, A., Krüger, S., and Rösch, N. (2013) Structure of Pd/Au alloy nanoparticles from a density functional theory-based embedded-atom potential. *The Journal of Physical Chemistry C*, **117**, 21810–21822.
- [24] Okamoto, H. and Massalski, T. B. (1985) The Au–Pd (Gold–Palladium) system. *Bulletin of Alloy Phase Diagrams*, **6**, 229–235.
- [25] Kittel, C. (2005) *Introduction to Solid State Physics*. John Wiley & Sons, 8 edn.
- [26] Perdew, J. P., Burke, K., and Ernzerhof, M. (1996) Generalized gradient approximation made simple. *Phys. Rev. Lett.*, **77**, 3865–3868.
- [27] Tyson, W. and Miller, W. (1977) Surface free energies of solid metals: Estimation from liquid surface tension measurements. *Surface Science*, **62**, 267 – 276.
- [28] Diehm, P. M., Ágoston, P., and Albe, K. (2012) Size-Dependent Lattice Expansion in Nanoparticles: Reality or Anomaly? *ChemPhysChem*, **13**, 2443–2454.
- [29] Pohl, J., Stahl, C., and Albe, K. (2012) Size-dependent phase diagrams of metallic alloys: A Monte Carlo simulation study on order–disorder transitions in Pt–Rh nanoparticles. *Beilstein Journal of Nanotechnology*, **3**, 1–11.

-
- [30] Enkovaara, J., et al. (2010) Electronic structure calculations with GPAW: a real-space implementation of the projector augmented-wave method. *Journal of Physics: Condensed Matter*, **22**, 253202.
- [31] Walter, M., Häkkinen, H., Lehtovaara, L., Puska, M., Enkovaara, J., Rostgaard, C., and Mortensen, J. J. (2008) Time-dependent density-functional theory in the projector augmented-wave method. *The Journal of Chemical Physics*, **128**.
- [32] Gritsenko, O., van Leeuwen, R., van Lenthe, E., and Baerends, E. J. (1995) Self-consistent approximation to the Kohn-Sham exchange potential. *Phys. Rev. A*, **51**, 1944–1954.
- [33] Kuisma, M., Ojanen, J., Enkovaara, J., and Rantala, T. T. (2010) Kohn-Sham potential with discontinuity for band gap materials. *Phys. Rev. B*, **82**, 115106.
- [34] Larsen, A. H., Vanin, M., Mortensen, J. J., Thygesen, K. S., and Jacobsen, K. W. (2009) Localized atomic basis set in the projector augmented wave method. *Phys. Rev. B*, **80**, 195112.
- [35] Weissker, H.-C. and Mottet, C. (2011) Optical properties of pure and core-shell noble-metal nanoclusters from TDDFT: The influence of the atomic structure. *Phys. Rev. B*, **84**, 165443.
- [36] Barcaro, G., Sementa, L., Fortunelli, A., and Stener, M. (2014) Optical Properties of Pt and Ag–Pt Nanoclusters from TDDFT Calculations: Plasmon Suppression by Pt Poisoning. *J. Phys. Chem. C*, **118**, 28101–28108.
- [37] Orendorff, C., Sau, T., and Murphy, C. (2006) Shape-Dependent Plasmon-Resonant Gold Nanoparticles. *Small*, **2**, 636–639.
- [38] López-Lozano, X., Barron, H., Mottet, C., and Weissker, H.-C. (2014) Aspect-ratio- and size-dependent emergence of the surface-plasmon resonance in gold nanorods – an ab initio TDDFT study. *Phys. Chem. Chem. Phys.*, **16**, 1820–1823.
- [39] López Lozano, X., Mottet, C., and Weissker, H.-C. (2013) Effect of Alloying on the Optical Properties of Ag–Au Nanoparticles. *J. Phys. Chem. C*, **117**, 3062–3068.

